Neutral beam injection simulations in the Wendelstein 7-X stellarator

Joona Kontula

School of Science

Thesis submitted for examination for the degree of Master of Science in Technology.

Espoo 17.8.2017

Thesis supervisor:

Prof. Mathias Groth

Thesis advisors:

D.Sc. (Tech.) Simppa Äkäslompolo

M.Sc. (Tech.) Jari Varje

Aalto University
School of Science

AALTO UNIVERSITY
SCHOOL OF SCIENCE

ABSTRACT OF THE
MASTER'S THESIS

Author: Joona Kontula

Title: Neutral beam injection simulations in the Wendelstein 7-X stellarator

Date: 17.8.2017 Language: English Number of pages: 6+41

Department of Applied Physics

Professorship: Fusion and Plasma Physics

Supervisor: Prof. Mathias Groth

Advisors: D.Sc. (Tech.) Simppa Äkäslompolo, M.Sc. (Tech.) Jari Varje

Stellarator fusion devices have seen a resurgence of interest in recent years, culminating in the building of the Wendelstein 7-X (W7-X) optimized stellarator in Germany. Compared to tokamaks, stellarators have the advantage of having no externally driven electric current. However, their non-axisymmetric nature makes it difficult to achieve closed particle orbits. The neutral beam injection (NBI) heating system will be a significant source of fast ions in W7-X, hence predictive modeling of the fast ion confinement is required for machine protection and scenario development. In this thesis, methods for numerical simulations of NBI ions in W7-X are established. Stellarator-specific magnetic field and radial electric field modules were implemented for ASCOT5, the latest development version of the Monte-Carlo orbit-following code ASCOT. Neutral beam injection in the W7-X high mirror ratio scenario was simulated with the BBNBI code, and subsequently the beam ion distribution and wall loads with ASCOT4. The results imply that the global confinement percentage of fast particles is higher than average, and the power loads low, in this scenario, although high local wall loads were also observed.

Keywords: Fusion, plasma, stellarators, fast ions, ASCOT

AALTO-YLIOPISTO
PERUSTIETEIDEN KORKEAKOULU

DIPLOMITYÖN
TIIVISTELMÄ

Tekijä: Joona Kontula

Työn nimi: Neutraalisuihkujen simuloiminen Wendelstein 7-X -stellaraattorissa

Päivämäärä: 17.8.2017 Kieli: Englanti Sivumäärä: 6+41

Teknillisen fysiikan laitos

Professuuri: Fuusio- ja plasmafysiikka

Työn valvoja: Prof. Mathias Groth

Työn ohjaajat: TkT Simppa Äkäslompolo, DI Jari Varje

Stellaraattori-tyyppiset fuusiolaitteet ovat viime vuosina tuottaneet yhä lupaavampia tuloksia, yhtenä tärkeimmistä Wendelstein 7-X stellaraattorin hyvin menestynyt ensimmäinen koekamppanja. Stellaraattorit ovat jatkuvatoimisia laitteita eivätkä vaadi ulkoisesti tuotettua plasmavirtaa, mutta niissä tarvitaan magneettikentän optimointia hiukkasten koossapidon varmistamiseksi. Erityisen vaarallisia ovat neutraalisuihkukuumennuksessa syntyvät nopeat ionit, joiden mallintaminen ennen kuumennuksen käyttöönottoa on tärkeää riskien kartoittamiseksi. Tässä työssä esittelemme menetelmiä neutraalisuihkujen mallinnukseen stellaraattoreissa. Stellaraattorien simuloimiseen vaadittavat magneetti- ja sähkökenttäominaisuudet lisättiin Monte Carlo-koodi ASCOT:n uusimpaan versioon. Neutraalisuihkujen toimintaa simuloitiin BBNBI-ohjelmalla, jonka jälkeen ionien ratoja seurattiin ASCOT4-ohjelmalla virtuaalisessa Wendelstein 7-X:ssä. Tulokset osoittivat, että nopeiden hiukkasten koossapito tutkituilla asetuksilla on kohtuullisen hyvä, mutta ionit saattavat paikallisesti aiheuttaa suuria seinäkuormia.

Avainsanat: Fuusio, plasma, stellaraattorit, nopeat ionit, ASCOT

Preface

It feels like my first summer slaving away for fusion at the "Science Factory" was ages ago, even though only three years have passed since then. Many people have given a helping hand on the way to this master's thesis. My supervisor Mathias Groth has been along for the journey from the beginning, and I'm grateful to him both for giving me the opportunity to work on fusion and also for being a true source of inspiration. My instructors on this thesis, Jari Varje and Simppa Äkäslompolo, have both been invaluable to the whole process, giving advice on ASCOT, stellarators, and beyond. Very special thanks go to Taina Kurki-Suonio, not only for the guidance and comments given for this thesis, but also for being a wonderful leader for the whole ASCOT group in general.

To my dear parents, Sirkka and Lasse, thank you for always supporting me on whatever I set out to do in the world. And of course, sometimes I would hardly be able to get out of bed in the morning, let alone write a thesis, without you, Stina.

Any work on Wendelstein 7-X would of course be impossible without the W7-X team in Greifswald. The plasma backgrounds and NBI geometries used in this thesis were provided by Yuri Turkin, the NBI parameters by Norbert Rust and the wall geometry by Sergey Bozhenkov. Some of the calculations in this thesis were performed on Marconi-Fusion, the High Performance Computer at the CINECA headquarters in Bologna (Italy). The computational resources provided by Aalto Science-IT project are also acknowledged. This work was partially funded by the Academy of Finland project No. 259675. This work has been carried out within the framework of the EUROfusion Consortium and has received funding from the Euratom research and training programme 2014-2018 under grant agreement number 633053 [and from Tekes – the Finnish Funding Agency for Innovation under the FinnFusion Consortium]. The views and opinions expressed herein do not necessarily reflect those of the European Commission.

Espoo, 17.8.2017

Joona Kontula

Contents

Symbols and abbreviations

Symbols

$\boldsymbol{B}$	magnetic flux density
$\boldsymbol{A}$	magnetic vector potential
$\boldsymbol{E}$	electric field strength
Φ	electric potential
e	elementary charge
ι	rotational transform
ω	angular frequency
R_0	major radius of a torus
r_0	minor radius of a torus
ρ	square root of normalized toroidal flux
θ	poloidal coordinate
φ	toroidal coordinate

Operators

$\frac{\mathrm{d}}{\mathrm{d}t}$	derivative with respect to variable t
$\frac{\partial}{\partial t}$	partial derivative with respect to variable t
$\sum_i$	sum over index i
$\boldsymbol{A} \cdot \boldsymbol{B}$	dot product of vectors $\boldsymbol{A}$ and $\boldsymbol{B}$
$\nabla \boldsymbol{A}$	gradient of vector $\boldsymbol{A}$
$\nabla \cdot \boldsymbol{A}$	divergence of vector $\boldsymbol{A}$
$\nabla \times \boldsymbol{A}$	curl of vector $\boldsymbol{A}$
$\hat{\boldsymbol{a}}$	unit vector in the direction of $\boldsymbol{A}$
$\dot{a}$	time derivative of a
$\ddot{a}$	second time derivative of a

Abbreviations

W7-X	Wendelstein 7-X
NBI	neutral beam injection
ICRH	ion cyclotron resonance heating
LCFS	last closed flux surface
PINI	positive ion neutral injector

1 Introduction

One of the most fundamental and perhaps the most important natural resource on earth is energy. Advancements in technology have allowed mankind to reach new heights in quality of life and scientific progress, but have resulted in a constantly growing demand for energy. Fundamentally, almost all energy sources that mankind has harnessed trace their roots back to the sun, which provides earth with a constant source of energy. The power source of the sun itself is *nuclear energy*. Usually nuclear energy is associated with the splitting of an atom's nucleus, or *nuclear fission*. Conversely, the power supply of the sun is *nuclear fusion* of hydrogen.

Fusion energy is based on the energy released in fusing together light atomic nuclei, usually the isotopes of hydrogen. Due to the abundance of hydrogen fuel on earth, nuclear fusion could potentially provide a nearly limitless supply of power, without the risk of radioactive wastes or proliferation associated with fission. However, the task of sustaining a fusion reaction on earth has proved to be challenging, with extreme temperatures and perfect plasma control required for success.

One approach to achieving conditions suitable for fusion is constructing a magnetic cage. As the fusion fuel consists of charged particles, they follow magnetic field lines and are thus confined in the magnetic cage [1]. This approach is called *magnetic confinement fusion*. Promising advances in the field of magnetic confinement fusion have been made, starting from humble beginnings in the 1950s to the 16.1 MW of fusion power achieved by the JET experiment in 1997 [2]. The most notable magnetic confinement fusion project at the moment is the building of the ITER test reactor in Cadarache, France [3]. ITER aims to demonstrate the feasibility of the magnetic confinement fusion concept to achieve a burning deuterium-tritium plasma, which would pave the way for a future fusion power plant.

Magnetic confinement fusion research has long been dominated by the torus-shaped *tokamak* concept. Tokamaks have the benefit of a simple axially symmetric geometry, which makes them relatively simple to construct. The inherent symmetries in the device also help in achieving a sufficiently high confinement time for both energy and charged particles. However, the toroidal plasma current used to achieve a helical magnetic field in tokamaks results in instabilities, and the transformer action commonly used to generate the plasma current limits tokamaks to pulsed operation.

Stellarators abandon the toroidal symmetry and toroidal current drive of tokamaks, and instead rely on the external magnetic field coils alone for helicity. The stellarator concept was invented in the 1950s by Lyman Spitzer [4], and predates the tokamak concept. The steady-state nature of stellarators makes them a promising concept for a future fusion power plant. Although stellarators have previously suffered from poor plasma performance compared to tokamaks, advances in supercomputing have allowed new, advanced stellarators to be designed. These devices are numerically optimized to achieve magnetic configurations with good confinement properties, and the gap between tokamak and stellarator performance is closing.

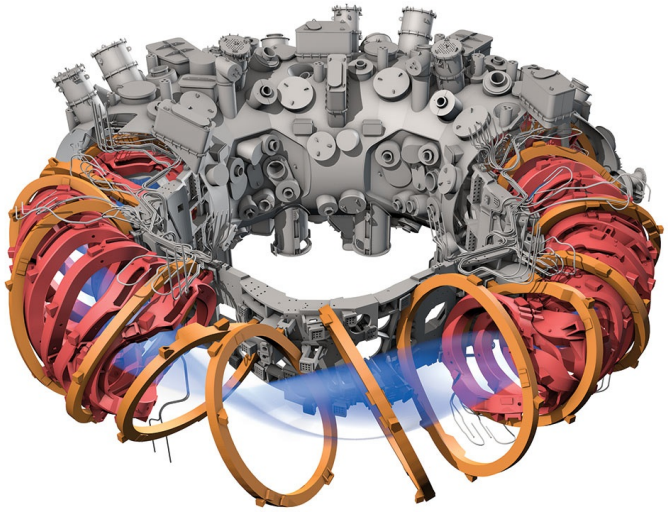

Figure 1: Wendelstein 7-X schematic view showing the plasma, modular coils, and vacuum vessel [12].

Since the 1950s, a large number of stellarator experiments have been conducted. These include HSX [5] in the USA, LHD in Japan [6], TJ-II in Spain [7], and the long-running succession of Wendelstein devices in Germany [8, 9].

Wendelstein 7-X (W7-X) is the largest and most advanced stellarator experiment in the world, operating at the Max-Planck-Institut für Plasmaphysik in Greifswald, Germany [10]. The exotic magnetic coil geometry of W7-X, shown in figure 1, is a result of many years of magnetic field optimization using supercomputers, and allows tailoring of the magnetic field to a plethora of configurations. W7-X began operations in 2015, meeting and even exceeding many of the goals for its first operational phase [11].

One of the major disadvantages of stellarators is the difficulty of achieving confined particle orbits. In tokamaks, the intrinsic axial symmetry of the device ensures that the particle orbits are closed, but stellarators require careful optimization of the magnetic field to prevent particle losses. Confinement in stellarators is particularly poor for fast ions due to their wide banana orbits. Because of this, demonstrating good confinement of fast ions is an important goal of W7-X. Fast ions in W7-X will be those produced in ion heating, such as neutral beam injection (NBI) and ion cyclotron resonance heating (ICRH). It is also possible that the fast ion wall loads produced by these heating systems might pose an operational constraint for W7-X.

Predictive modeling of the W7-X NBI system is important because it allows identifying operational scenarios with good fast ion confinement, as well as potential beam hot-spots, even before the commissioning of the NBI device. Such modeling can be done with a suitable 3D orbit-following Monte Carlo code, such as ANTS [13], BEAMS3D [14], or ASCOT [15]. ASCOT is a suite of codes developed in Aalto University for Monte Carlo simulation of minority particles in fusion plasmas. The code accepts

arbitrarily complex wall and magnetic field data, making it useful for detailed particle loss studies. Neutral beam injection can also be simulated in great detail using the NBI ionization code BBNBI [16], likewise developed at Aalto. Implementation of ASCOT for stellarators began in 2014, and ASCOT has already been proven to be a powerful tool for fast ion simulations in W7-X [17].

Since ASCOT is a computational tool, it has to keep up with recent advances in computer development. One major paradigm shift in computational physics has been the adoption of massively parallel computing, using GPUs and accelerator cards. This is the main motivation behind the development of ASCOT5, the new version of ASCOT.

In this thesis, a method for computationally studying the Wendelstein 7-X neutral beam injection system is presented. An introduction to the physical basis for the confinement of fast particles in stellarators, as well as the basic features of the W7-X stellarator, is given in section 2. In section 3, the computational methods used for simulating neutral beam injection in W7-X are established: namely, the neutral beam ionization code BBNBI and the Monte Carlo orbit following code ASCOT. The virtual model of W7-X used for computational studies is introduced, including the NBI device features. In section 4, the radial electric field and stellarator-specific magnetic field features are implemented for ASCOT5, and benchmarked against the previous version of the code, ASCOT4. A BBNBI simulation of the neutral beam injection in the W7-X high mirror ratio scenario is performed and studied. Finally, a simulation of the beam ions is done with the ASCOT4 code, and the particle confinement as well as the beam wall loads are analyzed. Conclusions from the simulations and possible avenues for future work are provided in section 5.

2 Why is it difficult to confine fast ions in stellarators?

2.1 Plasma and charged particle motion

Plasma is often called the fourth state of matter, distinct from the well-known solid, liquid and gaseous states. In a plasma state, the kinetic energy of electrons is high enough so that they are partially or completely dissociated from atomic nuclei, forming a mixture of positively charged ions and negatively charged electrons. The abundance of freely moving charge carriers in plasmas makes them highly susceptible to both external and internal electromagnetic fields, and the charged particles in the plasma are constantly interacting with each other. These properties distinguish plasmas from other states of matter.

Plasma physics is an extensive field of study, and a comprehensive review of plasma physics is beyond the scope of this thesis. The following is thus only an abridged introduction to plasma physics. Further reading of general plasma physics may be found in [18], while [19] is focused specifically on plasmas in stellarators. A good tokamak-focused treatment of plasmas can be found in [1].

Generally, plasmas are *quasi-neutral*, which means that the sum of positive and negative charges in the plasma is zero. This condition is only satisfied globally: the distance within which quasi-neutrality is not satisfied and the plasma constituent particles significantly interact with each other is called the *Debye length*. The Debye length is often used in approximations to distinguish bulk plasma phenomena from individual particle interactions.

One field of physics where plasmas are encountered frequently is *nuclear fusion*. Nuclear fusion energy (as well as fission energy) is based on the fact that the *nuclear binding energy* – the energy holding the nucleus together – per nucleon is dependent on the number of nucleons in the atom. In nuclear fusion, two light atomic nuclei are combined into a heavier nucleus. When the fusing nuclei are light, the total mass of the resulting nucleus is smaller than the sum of the two fusing nuclei. The difference in energy is released as photons and kinetic energy of the reaction products, such as α-particles or neutrons.

The enormous mass of the sun causes a gravitational pull strong enough to confine particles for a long time, which produces suitable conditions for self-sustaining fusion. The big question in fusion energy is how to achieve sufficient density, confinement, and temperature for self-sustaining fusion in terrestrial conditions. One approach to this problem is *magnetic confinement fusion*. Magnetic confinement of a plasma is based on the fact that charged particles experience the *Lorentz force*

$$\boldsymbol{F} = m\ddot{\boldsymbol{r}} = q(\boldsymbol{E} + \boldsymbol{v} \times \boldsymbol{B}), \tag{1}$$

where $\boldsymbol{r}$, q and $\boldsymbol{v}$ are the position, charge and velocity of the particle, and $\boldsymbol{E}$ and $\boldsymbol{B}$ are the electric and magnetic fields, respectively.

The dominant motion resulting from the Lorenz force is a rapid gyration of the particle around a magnetic field line, while the long time scale motion takes place along the field lines. Additionally, the particle may undergo drift motion perpendicular to the field lines. The frequency and radius of the particle gyromotion are [18]

$$\omega_c = \frac{|q|B}{m}, \tag{2a}$$

$$r_L = \frac{mv_\perp}{|q|\,B}, \tag{2b}$$

respectively, with $v_\perp$ being the particle velocity perpendicular to the magnetic field. These quantities are called the *cyclotron frequency* and *Larmor radius*, respectively. Furthermore, as the charge of the particle is moving in a roughly circular loop, the gyro-orbit can be viewed as an electric current loop. Consequently, the gyro-orbits has a corresponding *magnetic moment* $\boldsymbol{\mu}$, defined as the current I in the loop times the area A of the current loop [18]:

$$\boldsymbol{\mu} = IA\hat{\boldsymbol{n}} = I\pi r_L^2\hat{\boldsymbol{b}} = \frac{mv_\perp^2}{2B}\hat{\boldsymbol{b}}, \tag{3}$$

where $\hat{\boldsymbol{n}}$ is the unit vector normal to the current loop, and $\hat{\boldsymbol{b}}$ is the magnetic field unit vector.

According to the "hairy ball theorem" [20], any surface that is at all points tangential to a non-vanishing vector field must assume the topology of a *torus*. To confine collisionless charged particles, that ideally should follow magnetic field lines exactly, a magnetic field thus has to be torus-shaped. Otherwise, the particles would leak out of the magnetic cage from the points where the magnetic field is perpendicular to the surface.

An circular torus can be characterized by its *major radius* and *minor radius*, denoted by R_0 and r_0, respectively. Imagining the torus as a hollow tube, R_0 is the distance from the symmetry axis of the torus to the center of the tube, and r_0 is the radius of the tube. It is often convenient to use a coordinate system where the origin is situated at the center of the tube. A natural set of coordinates for a circular torus is the *minor radius coordinate* r, the *poloidal angle* θ, and the *toroidal angle* φ. The definition of the toroidal coordinate system – as well as conventional cylindrical coordinates – is shown in figure 2.

To achieve a torus-shaped magnetic field, a set of toroidally arranged magnetic coils is used. An example of this are the red magnetic coils in figure 1. The resulting magnetic field can be decomposed to radial, poloidal and toroidal components:

$$\boldsymbol{B} = B_r\hat{\boldsymbol{r}} + B_\theta\hat{\boldsymbol{\theta}} + B_\varphi\hat{\boldsymbol{\varphi}}. \tag{4}$$

The basic force balance equation, given by Newton's second law, in a confined plasma is given by the condition

$$\nabla p = \boldsymbol{J} \times \boldsymbol{B}, \tag{5a}$$

$$\Rightarrow \boldsymbol{B} \cdot \nabla p = \boldsymbol{B} \cdot \boldsymbol{J} \times \boldsymbol{B} = 0, \tag{5b}$$

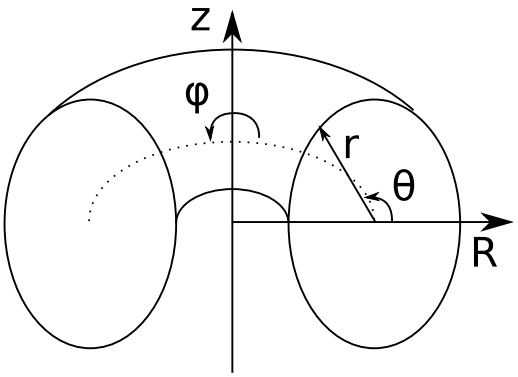

Figure 2: Explanation of the (r, θ, φ) coordinate system inside a torus, as well as the cylindrical coordinates (R, φ, z). Illustrated are the minor radius coordinate r, poloidal angle θ, and toroidal angle φ.

where p is the plasma pressure, $\boldsymbol{J}$ is the plasma current and $\boldsymbol{B}$ is the magnetic field [21]. This result implies that the plasma pressure is constant on magnetic field lines.

The magnetic field produced by the toroidal magnetic coils lies on nested isosurfaces of magnetic field strength called *flux surfaces*. The flux surfaces coalesce at the center of the tube at the so-called *magnetic axis*, where the poloidal component of the field is zero. The cross-section of flux surfaces and the shape of the magnetic axis are features that most strikingly distinguish stellarators from tokamaks. The tokamak magnetic field is *axisymmetric*, which means that the shape of the flux surfaces, as well as the location of the magnetic axis, are the same at all toroidal angles. Thus, the toroidal angle coordinate φ can be ignored for charged particle motion. The stellarator magnetic field possesses no axisymmetry, and the flux surface cross-section and magnetic axis location vary as functions of the toroidal angle. As an example, figure 3 shows the numerically calculated flux surfaces for one magnetic configuration of W7-X. The shape of the plasma changes from *bean-shaped* at $\varphi = 0°$ to *triangular* at $\varphi = 36°$.

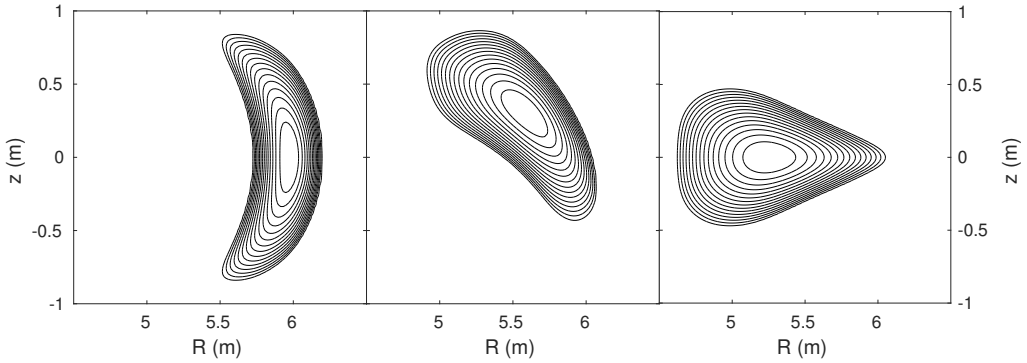

Figure 3: Flux surface contours of W7-X at three toroidal angles: $\varphi = 0°$, $\varphi = 18°$, and $\varphi = 36°$.

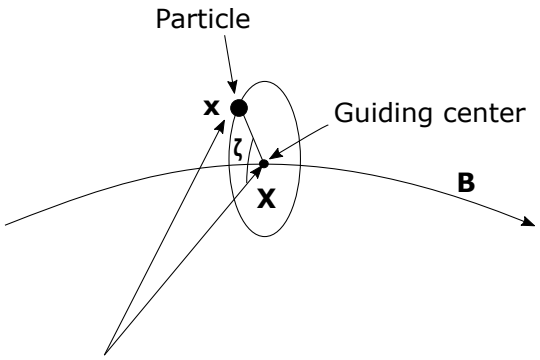

Figure 4: Definition of the particle and guiding-center positions ($\boldsymbol{x}$ and $\boldsymbol{X}$, respectively), as well as the gyroangle ζ, in a magnetic field.

Due to the force balance in the plasma (equation (5b)), flux surfaces have constant pressure, and in the center of the plasma particle transport parallel to $\boldsymbol{B}$ is fast enough to make the electron and ion temperatures constant as well [22]. In general, any function that is constant on flux surfaces is called a *flux function*. Eventually, the flux surfaces have to come in contact with the device walls. The last flux surface that can map out a closed contour within the boundaries of the device wall is called the *last closed flux surface* (LCFS).

2.2 Guiding-center motion and drifts

Due to the small Larmor radius of ions, and especially of electrons ($r_L \approx 0.1\,\mathrm{cm}$ and 0.1 mm, respectively), compared to typical device length scales (e.g. machine minor radius up to $r \approx 2.0\,\mathrm{m}$), the deviation of the exact particle location from the magnetic field line is not important in most situations. In this case, the variation in background plasma and magnetic field properties is negligible within the Larmor radius. In this case, one usually isolates the gyrating motion of the particle from the long time-scale motion, arriving at the *guiding center equations of motion* [23]. This transformation is applicable for both tokamaks and stellarators.

In the guiding center transformation, a conversion is done from the particle coordinates $\boldsymbol{z} = (\boldsymbol{x}, \boldsymbol{v})$ to the *guiding-center coordinates* $\boldsymbol{Z} = (\boldsymbol{X}, p_\parallel, \mu, \zeta)$, where $\boldsymbol{X}$ is the guiding-center position, $p_\parallel$ is the momentum parallel to the magnetic field, μ is the magnetic moment, and ζ is the guiding-center gyroangle. The relationship between the particle and guiding-center coordinates is illustrated in figure 4. Essentially, the guiding center position is in the center of the helical particle orbit, and includes all the information of the long time-scale motion of the particle.

In addition to the fast gyromotion and motion along the field lines, charged particles also undergo slow time-scale drift motion perpendicular to the magnetic field lines. One reason for this is that the magnetic field lines in a toroidal magnetic configuration are not straight. These deviations from straight field lines result in various drifts

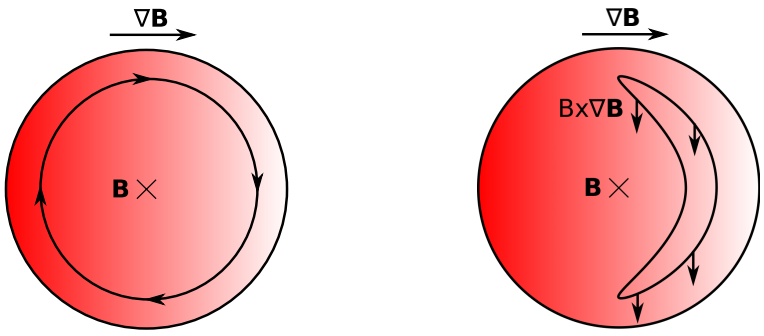

(a) (b)

Figure 5: Passing (a) and trapped banana (b) orbits in a magnetic field with a magnetic field gradient in the direction of the major radius coordinate $\boldsymbol{R}$.

effecting the guiding center trajectories of particles. Other drifts – which are not purely magnetic – include the $\boldsymbol{E} \times \boldsymbol{B}$, polarization, and diamagnetic drifts.

One important drift is that which a non-uniform magnetic field imposes to the guiding center velocity:

$$\boldsymbol{v}_{\nabla B} = \frac{m v_\perp^2}{2qB} \frac{\boldsymbol{B} \times \nabla B}{B^2} \tag{6}$$

This drift is called the ∇B *drift* [23]. The magnetic coils forming the confining magnetic field are packed closer together at the center of the torus, which inevitably results in the fact that

$$|B| \propto \frac{1}{R}, \tag{7}$$

where $|B|$ is the magnetic field magnitude and R is the distance from the center of the torus. Thus $\nabla B \parallel \hat{\boldsymbol{R}}$, and the direction of $\boldsymbol{B} \times \nabla B$ is either upwards or downwards, depending on the direction of the magnetic field.

Most of the guiding-center orbits are *passing orbits*, which means that they complete full toroidal rotations around the device: this type of orbit is shown in figure 5a. However, since both the magnetic moment $\mu = \frac{m v_\perp^2}{2B}$ and the kinetic energy $E_{\text{kin}} = \frac{1}{2} m v_\parallel^2 + \frac{1}{2} m v_\perp^2$ are constants of motion, it can happen that the parallel velocity of a particle goes to zero as it moves to a region of higher magnetic field strength. The particle is then reflected, and moves back towards the region of lower magnetic field strength. Since $B \propto 1/R$ in toroidal magnetic fields, the particle thus gets trapped on the outboard side of the torus. The trapped orbit topology is further shaped by the vertical ∇B drift, which imposes a finite width to the orbit of the particle: the particle drifts towards the center of the torus when in the upper hemisphere, and away from the center of the torus when in the lower hemisphere. This process is illustrated in figure 5b. The result is a so-called *banana orbit*, with the banana width determined by the magnitude of the ∇B drift [18]. In an ideal axisymmetric device, the drift on the upper hemisphere exactly cancels the one on the lower hemisphere. The banana orbit is thus closed, and no net drift occurs for the trapped particle.

2.3 Rotational transform

The vertical ∇B drift is always in opposite directions for ions and electrons. If the magnetic field only has a toroidal component, the ions and electrons are eventually separated due to the ∇B drift, causing an electric current transverse to $\boldsymbol{B}$. This effect needs to be prevented to ensure plasma stability. One way to cancel out the ∇B drift is making particles rotate around the magnetic axis as they move along the magnetic field lines. This way the net drift of the particles vanishes over one toroidal cycle. Since the particles closely follow the magnetic field lines, it is of interest to establish a way of providing a poloidal twist to the magnetic field.

Rotational transform, or ι, is defined as the average rotational angle of field lines after infinite toroidal circuits, divided by 2π: [19]

$$\iota = \lim_{N\to\infty} \frac{\sum_{k=1}^{N} \delta\theta_k}{2\pi N} \tag{8}$$

Claude Mercier was the first to derive an analytical expression for ι in the vicinity of the magnetic axis [24], showing that ι is given by

$$\iota = \frac{1}{2\pi} \int_0^L \left[\frac{\mu_0 J}{2B_0} - (\cosh\eta - 1)\, d' - \tau \right] \frac{\mathrm{d}l}{\cosh\eta} - N, \tag{9}$$

where $\mathrm{d}l$ is a differential length along the magnetic axis, J and B_0 are the current density and magnetic field on this axis, $e^{\eta} = r_2/r_1$ is the elongation of the flux surfaces, $d(l)$ the flux surface tilting angle with respect to the curvature vector $\boldsymbol{\kappa} = \mathrm{d}\hat{\boldsymbol{b}}/\mathrm{d}l$, and $\tau(l) = (\mathrm{d}\boldsymbol{\kappa}/\mathrm{d}l) \cdot (\hat{\boldsymbol{b}} \times \boldsymbol{\kappa})/\kappa^2$ is the torsion of $\boldsymbol{\kappa}$. The constant N is based on plasma topology and μ_0 is the vacuum permeability. This equation generally holds if the flux surfaces have an elliptical cross section, which is usually true close to the magnetic axis in stellarators.

As first pointed out by Spitzer [4], equation (9) implies there are three ways to provide rotational transform in a plasma:

1. running an induced current through the plasma;
2. rotating the flux surfaces when advancing around the torus;
3. making the magnetic axis non-planar.

The first one of these methods is used in tokamaks, while stellarators conventionally apply a combination of the last two methods, with some stellarators also utilizing the first.

One way to do achieve a toroidal plasma current is using a *transformer action*. In this approach, a current is run through a primary transformer winding, with the transformer core running through the center of the torus. The plasma itself acts as the secondary winding of the transformer, and a current is induced in the plasma according to Faraday's law [1]. An important caveat of this method is that it requires a time-dependent current in the primary winding. Because the current in the

winding cannot grow indefinitely, the transformer action is limited to pulsed operation. Another method of external current drive is toroidal acceleration of charged particles, which results in a fast particle driven toroidal current. The accelerated particles can be either the bulk plasma electrons or ions, or particles injected tangentially into the plasma [1].

2.4 Particle confinement in stellarators

The main reason for the dominance of the tokamak concept in magnetic confinement fusion is the historically poor plasma confinement of stellarator experiments. The difference in confinement properties between tokamaks and stellarators can be explained by *Noether's theorem*. This theorem states that for each symmetry in the Lagrangian of the system, there exists a constant of motion. Having a symmetry in the Lagrangian implies the existence of an ignorable coordinate. For axisymmetric systems, where the magnetic field strength is independent of the toroidal coordinate φ, Noether's theorem implies that the canonical toroidal momentum, defined as

$$p_\varphi \equiv R\left(mv_\varphi + eA_\varphi\right), \tag{10}$$

is a constant of motion [25]. Here m and v_φ are the particle mass and toroidal velocity, e is the elementary charge, and A_φ is the toroidal component of the magnetic vector potential.

If the particle energy, magnetic moment and toroidal particle momentum are conserved, as is the case with axisymmetric fields, it can be shown that the radial deviation of the guiding center from the field line is of the order $\delta\rho \approx r_B$, or the guiding center banana width. This result is known as Tamm's theorem, and is the basic premise for confinement in axisymmetric systems, where the radial drift of the particles is generally limited by the banana width [25].

Axisymmetric fields are a subset of *quasisymmetric* fields, where the magnetic field strength depends only on one angular coordinate when moving along a flux surface [22]. An even wider class of *omnigenous* fields also exists, for which the time-averaged radial drift of the particles vanishes even without quasisymmetry. In an omnigenous field, the contours of minimum magnetic field strength are either poloidally, helically, or toroidally closed [22]. For an axisymmetric field, omnigeneity is realized because the minimum magnetic field is always at the middle of the outer edge of the torus, and the contour is toroidally closed. Quasisymmetric and omnigenous fields are important for stellarator optimization, since they ideally enable perfect confinement in the absence of collisions.

An important caveat of quasisymmetric and omnigenous fields is that such fields only exist up to second order in *inverse aspect ratio* $\epsilon = 1/A = r_0/R_0$, where R_0 and r_0 are the machine major and minor radius, respectively. To a third order in ϵ, such fields cannot exist according to theory, but due to the usually large aspect ratio of stellarators this is not a significant problem in practice [22]. Practical stellarators

therefore rely on a good enough approximation of quasisymmetry or omnigeneity for confinement.

The redeeming factor for stellarators is that they offer a wide range of parameters to optimize the device performance [26]. First of all, the exact shape of the magnetic coils confining the stellarator plasma can be optimized using numerical methods. In addition, the coil currents can be adjusted, and additional control coils included in the assembly for controlling more magnetic field properties. For example, in the Wendelstein 7-X stellarator there are five identical sectors, each with 5 main field coils and 2 auxiliary coils, and the current in each one of these can be adjusted separately. This allows using one set of coils to achieve many different configurations [27].

2.5 Radial coordinates in tokamaks and stellarators

Many of the defining physical parameters of stellarators – such as electric potential and pressure – are approximately flux functions. As such, they can easily be represented by 1D profiles, as long as a suitable radial coordinate is chosen to map them to the flux surfaces. A wide array of radial coordinates is used in tokamak and stellarator literature, sometimes ambiguously. As such, an overview of different coordinate systems encountered in literature is provided here. The naming conventions for radial coordinates in tokamaks and stellarators, as well as those used in the stellarator equilibrium code VMEC [28], are shown in table 1. For the coordinate system in stellarators, this thesis follows the convention used by P. Helander [22].

Table 1: Radial coordinates used in tokamaks and stellarators, as well as the corresponding coordinates in the stellarator equilibrium code VMEC

Coordinate	Tokamak	Stellarator	VMEC
Toroidal flux	ψ_{tor}	ψ	φ
Normalized toroidal flux	$\psi_{\mathrm{tor,norm}} = \frac{\psi_{\mathrm{tor}} - \psi_{\mathrm{tor}}(\mathrm{axis})}{\psi_{\mathrm{tor}}(\mathrm{separatrix}) - \psi_{\mathrm{tor}}(\mathrm{axis})}$	$\psi_{\mathrm{norm}} = \frac{\psi - \psi(\mathrm{axis})}{\psi(\mathrm{separatrix}) - \psi(\mathrm{axis})}$	s
Square root of normalized toroidal flux	$\rho_{\mathrm{tor}} = \sqrt{\psi_{\mathrm{tor,norm}}}$	ρ	$\sqrt{s}$
Minor radius coordinate	r	$r_{\mathrm{eff}} = a\rho$	
Poloidal flux	ψ_{pol}	χ	
Normalized poloidal flux	$\psi_{\mathrm{pol,norm}} = \frac{\psi_{\mathrm{pol}} - \psi_{\mathrm{pol}}(\mathrm{axis})}{\psi_{\mathrm{pol}}(\mathrm{separatrix}) - \psi_{\mathrm{pol}}(\mathrm{axis})}$	$\chi_{\mathrm{norm}} = \frac{\chi - \chi(\mathrm{axis})}{\chi(\mathrm{separatrix}) - \chi(\mathrm{axis})}$	
Square root of normalized poloidal flux	$\sqrt{\psi_{\mathrm{pol,norm}}}$	$\sqrt{\chi_{\mathrm{norm}}}$	

Toroidal flux ψ, in both tokamaks and stellarators, is defined as the magnetic flux through an isosurface of the toroidal angle φ, whereas the poloidal flux χ is defined as the magnetic flux through an isosurface of the poloidal angle θ. The definitions of these fluxes are illustrated in figure 6. These quantities are then normalized, so that $\psi_{\mathrm{norm}}, \chi_{\mathrm{norm}} = 0$ at the magnetic axis and $\psi_{\mathrm{norm}}, \chi_{\mathrm{norm}} = 1$ at the LCFS. Often, a square root is taken of the toroidal and poloidal flux, denoted by $\rho_{\mathrm{tor}} = \sqrt{\psi_{\mathrm{norm}}}$

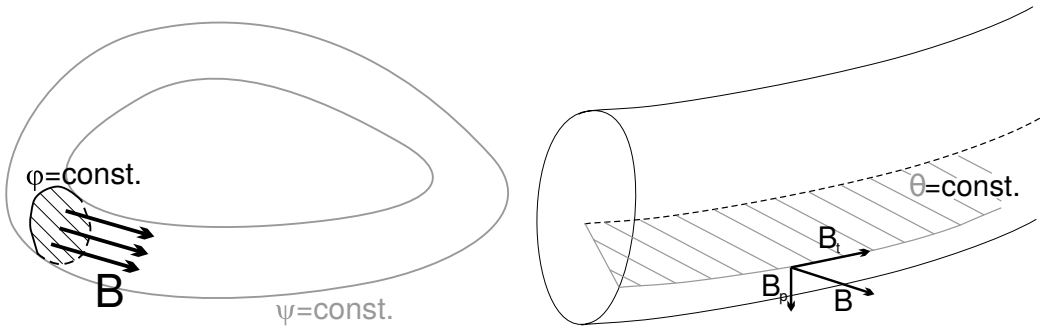

(a) (b)

Figure 6: Illustration of the definition of toroidal flux ψ (a) and poloidal flux χ (b) in tokamaks and stellarators [22].

and $\rho_{\text{pol}} = \sqrt{\chi_{\text{norm}}}$. Using ρ_{tor} or ρ_{pol} results in a more linearly distributed radial coordinate, because they are both measured through an area which grows roughly as r^2. Although the minor radius r_0 is not well defined for stellarators, a similar quantity can be approximately defined. The *effective minor radius* a can be approximated from the relation

$$V_{\text{plasma}} \approx 2\pi R_0 \cdot \pi a^2. \tag{11}$$

2.6 Stellarator symmetry

The magnetic field geometry of stellarators is not axisymmetric. However, stellarator magnetic fields can be designed to have other symmetries, which can be used to simplify the magnetic field design. A commonly used symmetry in the field geometry of stellarators is the *stellarator symmetry* [29]. Unlike quasisymmetry and omnigeneity, which are design goals of the (non-axisymmetric) magnetic field, stellarator symmetry is a man-made feature. In a stellarator symmetric device, the magnetic field is divided into n identical sectors. Each of these sectors possesses special symmetry with regards to the center of the sector, $\varphi_0 = 0$, as well as the edges of the sector. For a scalar field V, this symmetry can be expressed in cylindrical coordinates as

$$V\left(R, z, \varphi\right) = V\left(R, -z, -\varphi\right) \tag{12}$$

and for a vector field $\boldsymbol{V}$ as

$$\left(V_R, V_\varphi, V_z\right)\Big|_{(R,\varphi,z)} = \left(-V_R, V_\varphi, V_z\right)\Big|_{(R,-\varphi,-z)} \tag{13}$$

The number of toroidal sectors has no significance for the plasma properties, and depends on the reactor design [29]. For example, W7-X has a 5-fold stellarator symmetry, which means only a tenth of the magnetic field information is needed for full representation. An example of stellarator magnetic fields with a different number of toroidal sectors is shown in figure 7.

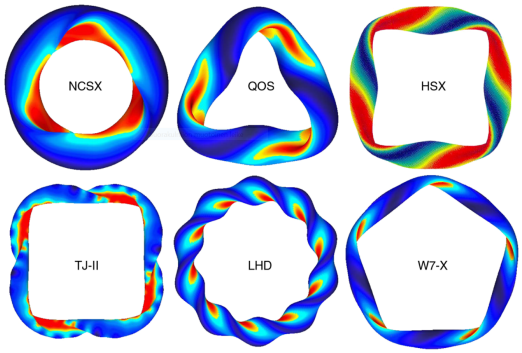

Figure 7: Examples of stellarators with different number of symmetric magnetic field sectors [30]. The number of symmetric sectors are three for NCSX and QOS, four for HSX and TJ-II, ten for LHD and five for W7-X.

2.7 Influence of electric fields on particle confinement

Although no external toroidal current is driven in stellarators, intrinsic sources of currents still exist. *Bootstrap current* is a plasma current resulting from radial pressure gradients in the plasma, in accordance to the force balance equation (5b). In tokamaks, where the desired ι is achieved by driving a current in the plasma, bootstrap current provides an intrinsic means of gaining additional rotational transform. In stellarators, on the other hand, bootstrap current can disturb the magnetic equilibrium, creating magnetic islands and altering the location of plasma-wall interactions. Optimizing and compensating to achieve low bootstrap current is thus necessary for successful stellarator operation [31].

In addition to the toroidal bootstrap current, stellarators can also have radial electric currents, which are related to the *radial electric field* $\boldsymbol{E}_{\text{rad}}$. The radial electric field can be derived from the radial component of the equilibrium force balance (equation (5b)) [32]. Unlike the toroidal electric current, a radial electric field can improve stellarator performance. In stellarators, a low collisionality regime of high radial diffusion exists for fast particles. This is caused by fast particles getting trapped in local magnetic wells, such as between two magnetic coils. The radial electric field gives rise to a poloidal $\boldsymbol{E}_{\text{rad}} \times \boldsymbol{B}$ drift that guides the particles to different trapped regions, perturbing the radial drift and thus improving fast confinement [22].

Due to the high mobility of charge carriers along field lines, the electric potential is constant on flux surfaces and is thus a flux function of the radial coordinate ρ. The radial electric field is directly related to the electric potential and is given by

$$\boldsymbol{E}_{\text{rad}} = -\nabla\Phi(\rho) \tag{14a}$$

$$= -\frac{\partial\Phi}{\partial\rho}\nabla\rho. \tag{14b}$$

2.8 The Wendelstein 7-X stellarator

Wendelstein 7-X is an advanced stellarator, built and operated at the Max Planck Institute for Plasma Physics in Greifswald, Germany [10]. Instead of a separate set of toroidal and helical magnetic coils, as in classical stellarators, advanced stellarators use a set of modular coils designed to achieve a similar magnetic field as the two separate sets. W7-X is a successor to the Wendelstein 7-AS device, which was operated from 1988 to 2002 and also featured modular magnetic coils. W7-X assembly took place between 2009 and 2014, and first plasma was achieved in 2015. Compared to many classical stellarators, W7-X is characterized by its optimized modular coil structure. The magnetic geometry is shaped by 50 non-planar modular superconducting coils, creating a magnetic field that can reach up to 3.0 T on the magnetic axis [33]. The configuration can further be shaped by 20 planar magnetic coils. The scale of the W7-X experiment is on par with present day tokamaks, such as JET, although W7-X is restricted to hydrogen (H) and deuterium (D) operation. Tritium (T) operation was excluded from the W7-X experiment due to the high cost of tritium handling facilities. A detailed comparison of device parameters between W7-X, JET, and the next generation ITER reactor is shown in table 2.

Table 2: Main device parameters of the W7-X stellarator, compared to present day tokamak JET and future test reactor ITER [33, 34, 3].

Parameter	JET	W7-X	ITER
major radius (m)	3.0	5.5	6.2
minor radius (m)	0.9	0.53	2.0
plasma volume (m^3)	90	30	840
magnetic field (T)	3.5	2.5 to 3.0	5.3
heating power (MW)	50	15 to 30	73 to 110
pulse length (min)	<1	30	10
fuel mixture	H, D, T	H, D	H, D, T

One of the main goals of W7-X is to achieve steady-state plasma operation in a fusion device [33, 35]. Conceptually, steady-state operation is possible because no plasma current is used and thus no transformer action is required to run the device. However, the operational time is still technically limited to an estimated 30 min due to plant power exhaust issues. Nevertheless, W7-X still has much longer pulse lengths than any similarly-sized tokamak, and can thus give important insight into future fusion power plant design.

Heat exhaust in W7-X can be achieved by means of either a *limiter* or an *island divertor* approach. In the limiter scheme, which was used for the initial operation of W7-X, the plasma-wall interaction is focused on five limiter elements, located on the inboard side of the device. Toroidally, the limiter elements are situated at the bean-shaped region of the device, as shown in figure 8.

The island divertors are be the main method for power exhaust in the present

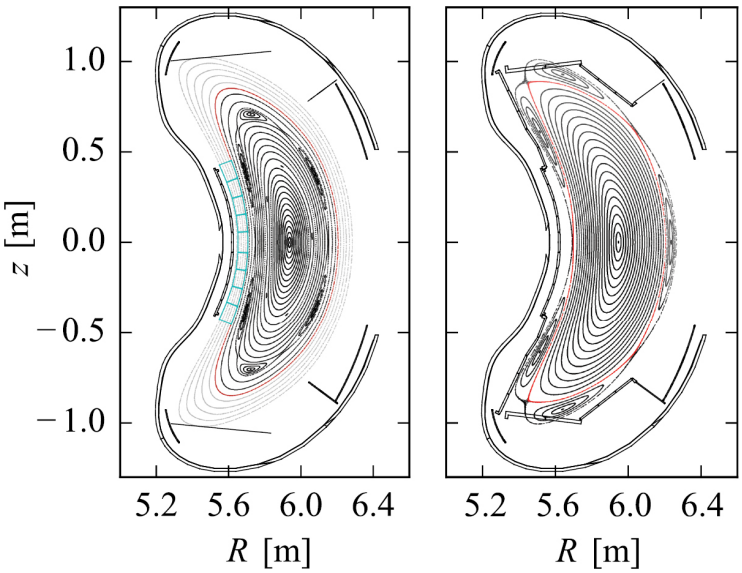

Figure 8: W7-X Limiter and divertor positions and magnetic field topology for the limiter configuration (left) and for the standard divertor configuration (right) [36]. The blue lines show the position of the limiter, and the black lines show the position of the island divertor structures and device wall.

operation of W7-X. There are a total of 10 divertor elements, located stellarator-symmetrically at the bean-shaped sections of high curvature. A naturally occurring chain of magnetic islands is used to divert the plasma to the island divertor, moving plasma-wall interaction further away from the core plasma [37]. The location of the divertor plates and magnetic islands in one configuration of W7-X is shown in figure 8.

The diagnostic systems of W7-X are comprehensive, and further upgrades are made as the experiment progresses [38]. Diagnostics include neutron counters, diamagnetic loops for plasma energy measurements [38], Rogowski coils for net current measurements [39], interferometers for density measurements [40], spectrometers for core plasma temperature and plasma rotation measurements [41], radiation measurements with bolometers [42], Thomson scattering diagnostics for electron density and temperature [43], and video diagnostics for plasma observation and protection from unintentional plasma wall interaction events [44].

2.9 Heating the plasma with neutral beam injection

The energy confinement of fusion plasmas is never perfect, and some energy is always leaking from the system. To sustain the high temperature, the energy losses have to be compensated by heating, which can come either from the fusion reactions in the plasma or from auxiliary heating. For a plasma in thermodynamical balance, a

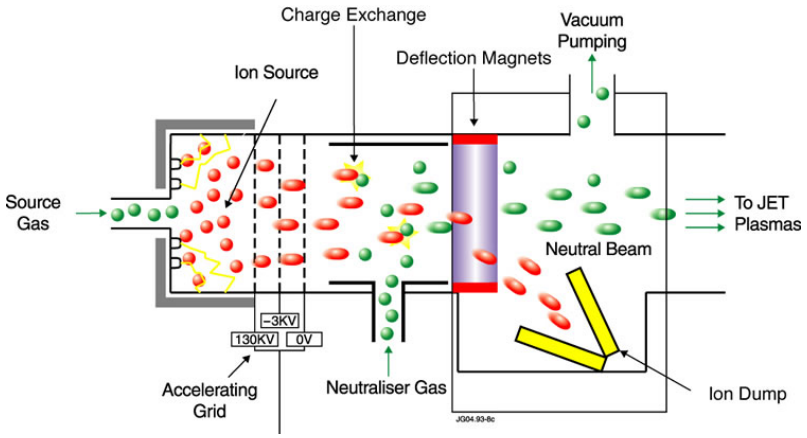

Figure 9: Schematic of the NBI operating principle in JET, which is similar to W7-X. The green spheres represent neutrals, and the red spheres ions [46].

simple power balance equation can be formulated:

$$P_\alpha + P_{\text{aux}} - P_{\text{loss}} = 0, \tag{15}$$

where P_α is the heating due to fusion-born α-particles, P_{aux} is the applied auxiliary heating, and P_{loss} is the energy lost due to conduction and radiation [1].

In present-day fusion experiments, the α-particle heating is negligible compared to the energy losses, so auxiliary heating is necessary to maintain the power balance. Furthermore, fusion reactions only start taking place at high temperatures, so auxiliary heating is always required for fusion start-up. Possible approaches to auxiliary heating are, e.g., *ion cyclotron resonance heating* (ICRH), *electron cyclotron resonance heating* (ECRH), and *neutral beam injection* (NBI).

In neutral beam injection, an energetic beam of neutral particles is injected into the plasma. When interacting with the plasma particles, they become ionized and start to experience electromagnetic forces in the plasma [45]. The goal of neutral beam injection is to produce a fast ion population near the center of the plasma. Additionally, the fast ion birth distribution has to be optimized so that the fast ions are confined for a sufficient time to deposit their kinetic energy to the plasma. This is achieved by injecting highly energetic neutrals that penetrate deep into the plasma, and optimizing the injection angle so that the ions are born on well-confined orbits.

The internal structure of a neutral beam injector is illustrated in figure 9. The neutral beam generation starts with the ionization of a neutral source gas. The ions are then accelerated by means of an electric field, giving them a predetermined kinetic energy. The accelerated particles are then again neutralized by charge exchange reactions with a neutralizer gas. A deflection magnet and vacuum pump are used to remove charged particles and neutralizer-gas residue, leaving only the desired neutral particles entering the plasma.

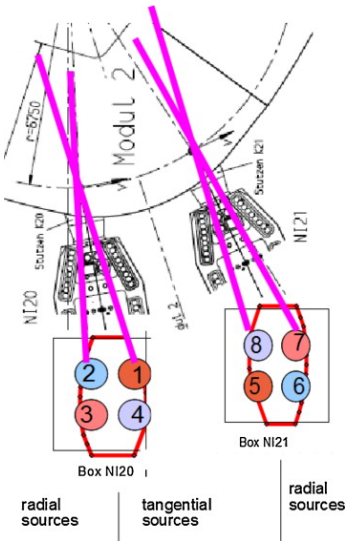

Figure 10: Simplified geometry of the W7-X NBI system [48]. The magenta lines show the beam directions for the different PINIs.

Due to the nature of the source-gas ionization process, a fraction of the ionized particles become part of molecules with the same charge state but with one to three hydrogen atoms. Since the electric field used to accelerate the particles is constant, this results in three energy components of the final accelerated hydrogen: $E_{\max}$, $E_{\max}/2$ and $E_{\max}/3$.

The neutral atoms entering the plasma are, with a certain probability, ionized by interactions with the electrons and ions in the plasma. They then effectively become a highly energetic part of the bulk plasma, and thus gradually deposit their high kinetic energy to the electrons and ions in the plasma [47]. The timescale at which this happens is characterized by the *slowing-down time* of the fast ions.

If a beam particle particle passes through the plasma without being ionized, it is called a *shine-through* particle. Shine-through particles could cause significant power loads to the components intersecting the beam lines, so protective plates and water cooling are often installed to the walls opposite the injectors.

The NBI system in W7-X is similar to that of ASDEX Upgrade [49]. There are two injection boxes, located symmetrically in one toroidal sector. Each injector is further divided into four separate *positive ion neutral injectors* (PINIs), each with different orientation. The beam acceleration is set at 55 kV, although operation at up to 100 kV is possible if upgrades are performed. The beam geometry is illustrated in figure 10. An important limitation is that the NBI system is designed for 10 second pulses of heating: this rules out using the NBI system as the steady-state heating mechanism for W7-X, where pulse lengths of up to 30 minutes are planned [48].

NBI operation in W7-X is planned to start with two PINIs in both of the two injection boxes. The total power of the four PINIs used in initial operation will be 6.84 MW. The detailed injector powers, injection angles, and injected isotopes are shown in

table 3. The beam injection in W7-X is almost perpendicular to the magnetic axis, deviating only 3.4° from completely perpendicular for the "radial" PINIs, and 11.6° for the "tangential" PINIs. This is due to the tightly packed modular coil structure of W7-X [50], and also has the benefit of avoiding unwanted toroidal current drive.

Table 3: NBI parameters for the commissioning of the NBI system in W7-X.

Injector	PINI	Injection angle (°)	Isotope	P (MW)
NI20	3	3.4	Hydrogen	1.78
NI20	4	11.6	Hydrogen	1.64
NI21	7	3.4	Hydrogen	1.78
NI21	8	11.6	Hydrogen	1.64

Due to the perpendicular NBI injection angle in W7-X, most of the beam ions are born on trapped orbits [27, 17]. In addition, most of the NBI particles are ionized near the last closed flux surface. This is caused by the "hollow" density profile of W7-X: the density has a high gradient near the LCFS, and does not peak noticeably at the magnetic axis. The beam deposition profile could be made more favorable by decreasing plasma density, but this causes problems with plasma performance and shine-through. The high fraction of trapped NBI ions combined with the unfavorable ionization profile could lead to high fast ion wall loads in W7-X.

An optimized scenario of special interest with regards to NBI ions is the *high mirror ratio* scenario. The mirror ratio is defined as

$$\frac{B(\varphi = 0°) - B(\varphi = 36°)}{B(\varphi = 0°) + B(\varphi = 36°)}, \tag{16}$$

where $\varphi = 0°$ corresponds to the bean-shaped plane where the magnetic curvature is largest [51]. This scenario was optimized particularly for good confinement of fast ions: the high mirror ratio keeps the toroidal range where the particles are reflected as narrow as possible, and the parallel velocity of the particles is thus constant for as long as possible [27].

3 Predicting the behavior of fast ions in stellarators

3.1 ASCOT – simulating minority particle populations

ASCOT (**A**ccelerated **S**imulation of **C**harged Particle **O**rbits in **T**ori) is a Monte Carlo code for simulating minority particles in a given plasma [15]. ASCOT numerically solves the kinetic equation for the distribution function f of a minority species:

$$\frac{\partial f}{\partial t} + \dot{\boldsymbol{z}} \cdot \frac{\partial f}{\partial \boldsymbol{z}} = \left(\frac{\partial f}{\partial t} \right)_{\text{coll}}, \tag{17}$$

where $\boldsymbol{z} = (\boldsymbol{x}, \boldsymbol{v})$. The right hand side is a *collision operator*, which includes collisional processes with the background plasma. Minority particles could, for example, be highly energetic hydrogen ions, impurity particles, or helium ash. Solving the kinetic equation by discretization, i.e. finite element methods, is difficult due to the 6 dimensions in the equation, and also because the physical boundary conditions for the distribution function are a large source of uncertainty. A more practical method is solving the kinetic equation by *Monte Carlo sampling* of individual particle motion.

In the Monte Carlo method, individual *test particles* whose motion is determined by a stochastic differential equation consistent with equation (17) are followed, and a steady-state solution for f is obtained by taking the average of the different realizations of the particle motion [52]. Each test particle is weighted in mass, charge etc. so that it represents a large number of physical particles. In this approach, the effect of the simulated minority particles on the bulk plasma properties, such as temperature or density, are neglected. As such, it is possible to simulate particles one at a time using a static background. ASCOT can utilize both full-orbit and guiding-center equations of motion, depending on the simulation requirements. A Monte-Carlo Fokker-Planck collision operator is used for evaluating the effects of Coulomb collisions [23].

As input, ASCOT requires the equilibrium magnetic field, which can be given in either 2D or 3D arrays, and the physical wall. Radial electric fields can be imposed as a 1D profile inside the LCFS. Plasma data, either 1D or 2D, includes densities and temperatures for electrons as well as for any number of background ion species. The initial locations and velocities of the test particles can be supplied either in particle or guiding-center coordinates.

One of the main advantages of ASCOT is that the magnetic background and wall geometry can be supplied in full 3D [15, 53, 54]. Many similar Monte Carlo codes are written for tokamaks, and thus assume axisymmetry. As a fully 3D code, ASCOT is suitable for simulating particles in both stellarators and tokamaks with 3D features.

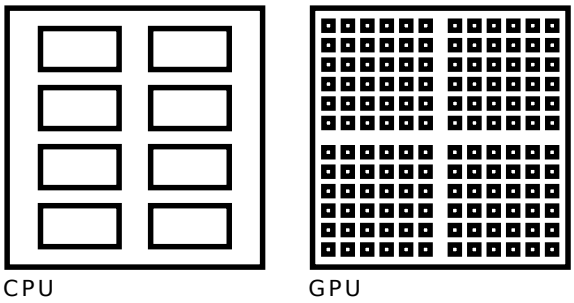

Figure 11: Conceptual difference between conventional and massively parallel computing. The big boxes represent one computing node, and the smaller boxes inside represent individual processes. On the left is a CPU with a few powerful cores executing a single process, and on the right is a modern processor with a large number simultaneous processes.

The main outputs of ASCOT are the distribution function of the minority particle species and the recorded positions and energies for possible wall hits. From the distribution function, different physical quantities can be derived, such as the power deposited to the different background plasma species, the current drive, and the fast ion loss fractions as a function of time. Optionally, the complete particle orbits can be recorded at specified intervals, although this is generally only done for special cases due to the large amount of output data produced.

The latest development version of ASCOT is called ASCOT5. Compared to previous versions of ASCOT, the most significant difference is that ASCOT5 is programmed in C, whereas the previous versions were implemented in Fortran. The main motivation for writing ASCOT5 was the emergence of massively parallel scientific computation. In the past, computation was generally done with a low number of parallel processes, usually in the order of 10 per computing node, and programmers have relied on the fast linear execution of commands for speed. Modern processor, on the other hand, are capable of executing multiple simultaneous *threads*, as well as processing arithmetic operations on multiple *vector elements* in one processor cycle [55]. This means that the number of parallel processes in modern CPUs is much larger: the difference is illustrated in figure 11. ASCOT is conceptually suitable for massively parallel computing, because the algorithm it uses is *embarrassingly parallel*: each test particle is followed independently, and no information is exchanged between processes.

3.2 BBNBI – generating the beam ions

Since one of the two major sources of fast ions in W7-X is the NBI heating system, a suitable method for simulating the ionization of beam neutrals must be used before fast particle simulations can be performed. The NBI simulation code BBNBI was specifically developed to satisfy the NBI generation needs of ASCOT [16]. To facilitate this, it is compatible with the I/O structures of ASCOT, ensuring consistency of

background data between particle generation and slowing down simulation. Although BBNBI was developed as a part of the ASCOT3 distribution, it is independent of the orbit following implementation. This meant that BBNBI did not have to be rewritten as a part of ASCOT5 development, but can be used as is with ASCOT5, or indeed with any other code.

In BBNBI, the NBI beam is modeled as a set of sub-beams, or *beamlets*, starting from the grounded grid. The beamlets are given a divergence value, describing the deviation of particles from the nominal direction of the beamlet. Upon entering the vacuum vessel, the particle is advanced until its ionization probability exceeds a random threshold λ, after which the exact ionization location is calculated and recorded. BBNBI has been verified against several established NBI simulation codes, and excellent agreement has been found for both tokamaks and stellarators [17, 16].

The input for BBNBI consists of the detailed injector geometries, including the beamlet directions, as well as the injection powers for the different PINIs. As an output, BBNBI produces the NBI ion distribution in space, with a particle weight indicating how many particles per second are generated at this location. The output also includes the shine-through particle energy and location.

3.3 Components for the virtual Wendelstein 7-X

W7-X plasma equilibria can be calculated by repeatedly iterating the VMEC, NTSS, and DKES codes [56, 57, 58, 28]. VMEC solves the 3D magnetohydrodynamic equilibrium, NTSS calculates the 1D plasma profiles, and DKES provides neoclassical coefficients for the NTSS calculation. The iterative approach ensures self-consistent modeling of the magnetic field and plasma profiles. NBI heating can be included in the plasma profile calculations inside NTSS. The output of these calculations are the 1D plasma profiles and the 3D magnetic field equilibrium inside the LCFS. The EXTENDER code is then used to calculate the magnetic field outside the LCFS [59].

The W7-X wall used for ASCOT simulations is based on CAD data from the W7-X component database [60]. It consists of over 4 million individual triangles, and includes all of the key components installed in the next operational phase of W7-X. A comparison of a camera image from W7-X and the ASCOT wall model, as seen from the same port, is shown in figure 12.

The operational scenario studied in this thesis uses the high mirror ratio magnetic field configuration [27]. This configuration is important with regards to NBI operation, because the scenario was originally thought to be good for fast ion confinement, and as such is one of the "standard" operational scenarios planned for W7-X.

Figure 13 shows the plasma density and temperature for the W7-X high mirror ratio scenario [61]. The density profile has a high gradient near the LCFS, but both the

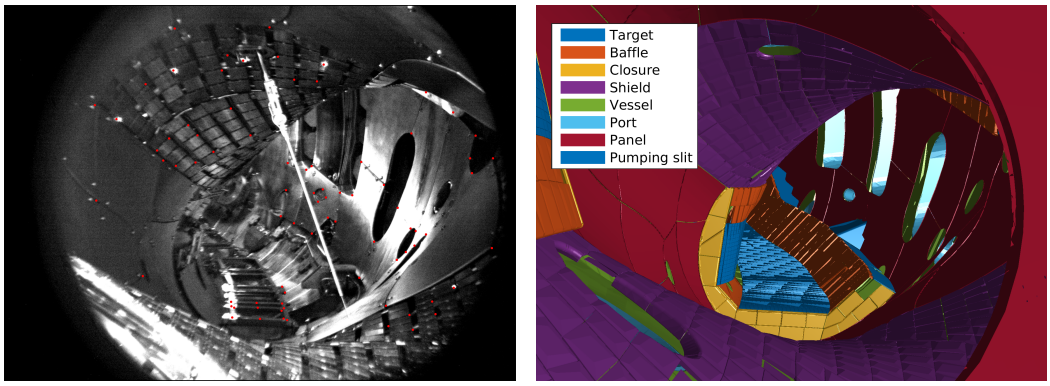

(a) (b)

Figure 12: Comparison of a visual camera image (a) and the complex wall model (b) of the W7-X vessel. The virtual camera is positioned at the exact location of the camera [60]. In the wall model picture, the most important different types of wall components are color-coded.

electron and ion density saturate at $\rho \approx 3/4$. This flat density profile is typical for W7-X plasmas. The electron density peaks at $n_e = 2.0 \times 10^{20}\,\mathrm{m}^{-3}$, and the ion density at $n_e = 1.8 \times 10^{20}\,\mathrm{m}^{-3}$. The temperature profile is not as flat as the density profile, although the gradients are still the highest near the LCFS. The maximum temperature for the electrons at $\rho = 0$ is $T_e = 1.42\,\mathrm{keV}$. The scenario also includes a radial electric field, which is given as a $(\frac{\partial \Phi}{\partial \rho}, \rho)$ profile.

It should be noted that the equilibrium simulations used for these profiles included one of the NBI sources at 1.7MW injected power as a heating source. On the other hand, no results from the NBI modeling by ASCOT are included in the equilibrium calculation. Any NBI modeling for these background plasmas is therefore not self-consistent, and realistically at best represents *beam blips*: short pulses of neutral beam injection that are non-perturbative to the background plasma equilibrium.

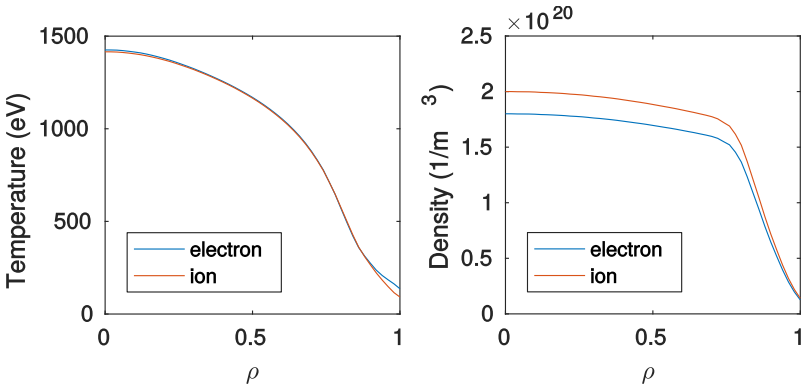

Figure 13: Electron and ion temperatures (left) and densities (right) for the W7-X high mirror ratio scenario.

4 Neutral beam performance in Wendelstein 7-X as simulated by ASCOT

4.1 Stellarator magnetic field in ASCOT5

The magnetic field data format for ASCOT5 is the HDF5 [62] file format. For tokamak 3D fields in ASCOT, the entire toroidal extent of the field is given as an input. The magnetic field for stellarators, on the other hand, can be given as point values on a regular cylindrical (R, φ, z) grid, for half a toroidal period. These values are for the equilibrium magnetic field, and are usually obtained from a magnetic equilibrium code such as VMEC. According to equations (12) and (13), half a toroidal period is enough to imply the full toroidal extent of the magnetic field.

To implement this type of magnetic field input for ASCOT5, the following scheme was followed:

1. Read the magnetic field data, calculated by some external tool, for half a period
2. Upon initialization, construct one complete toroidal period from the data
3. When evaluating the field, use $\varphi = \varphi \bmod (2\pi/n_{\text{periods}})$.

This way, stellarator symmetry is only called upon during initialization, and simple periodic boundary conditions can be used for interpolation. Due to this input format, a discrete formulation of equations (12) and (13) was needed. For a grid with dimensions $\left(n_R, n_\varphi, n_z\right)$, the stellarator symmetric indexes are given by

$$\left(i_R, i_\varphi, i_z\right) \Leftrightarrow \left(i_R, 2(n_\varphi - 1) - i_\varphi, n_z - i_z - 1\right). \tag{18}$$

In addition to the initialization routines, it was necessary to implement interfaces for evaluating the magnetic field and gradients, as well as the radial coordinate ρ and its gradient. These featured already existed for the 2D and 3D magnetic fields, but not for stellarator-symmetric fields. In addition, since the input formats for ASCOT4 and ASCOT5 are different, an interface was developed for reading ASCOT4-format HDF5 files and converting them into the ASCOT5 input format. Finally, testing routines were written for all of the magnetic field functions.

The version of ASCOT5 used in this thesis employs *local Hermite splines* for 3D interpolation. This scheme has limited accuracy: for example, when constructing the local splines it uses a rudimentary finite difference method for calculating derivatives of the interpolant. ASCOT4 uses globally constructed splines for interpolation, which are more accurate and are currently being implemented for ASCOT5 as well.

To test that the magnetic field was evaluated correctly, the evaluation was benchmarked against the previous version of the code, ASCOT4. Three 1D slices of the magnetic field domain – in the r, φ, and z directions – were calculated while keeping two of the coordinates constant. The constant coordinates ere chosen as

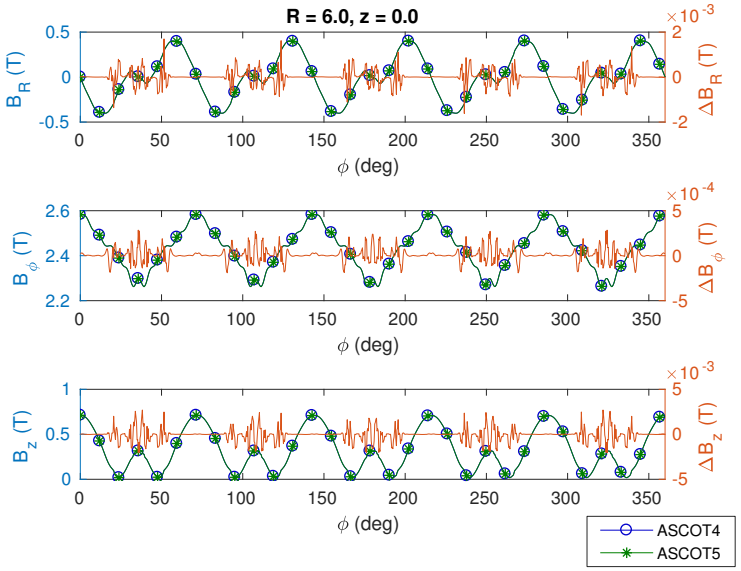

Figure 14: Profiles of the stellarator magnetic field $\boldsymbol{B}$ in the φ direction. The blue lines show evaluated values for ASCOT4, and the green lines show the evaluated values for ASCOT5. The orange line shows the absolute difference (ASCOT4 - ASCOT5) between the two lines. Note the different axis used for the difference.

($R = 6.0\,\mathrm{m}, \varphi = 72°, z = 0.0\,\mathrm{m}$). This choice of coordinates gives 1D profiles which generally fall inside the LCFS, but also pass through it to allow investigating the evaluation of the plasma edge. The magnetic field used was from the W7-X high mirror ratio scenario, and had grid dimensions of $n_R = 173, n_\varphi = 141$, and $n_z = 170$.

A comparison between the evaluated fields from ASCOT4 and ASCOT5 shows that the two codes agree very well with each other. The results of the magnetic field benchmarking in the φ direction are shown in figure 14. These φ direction profiles show the complete toroidal extent of the magnetic field. The biggest absolute difference of the components of $\boldsymbol{B}$ between the two codes are in the order of $10^{-3}\,\mathrm{T}$. Some of the differences between the two results are likely to be caused by the different interpolation methods used.

For the gradient of the magnetic field, the differences between ASCOT4 and ASCOT5 are relatively larger than for $\boldsymbol{B}$. Benchmarking results for the magnetic field gradient $\nabla\boldsymbol{B}$ in the φ direction are shown in figure 15. The absolute differences are largest at the maximum and minimum values of the gradient. However, the differences are still minor, and most likely due to the different interpolation methods used: in general, the interpolation of the derivatives is more sensitive to the method used.

The results of the $\boldsymbol{B}$ and $\nabla\boldsymbol{B}$ benchmarking in the R and z directions are shown in the appendix (appendix A.1, figures A1 to A4). The results in these directions were similar to the ones in the φ direction.

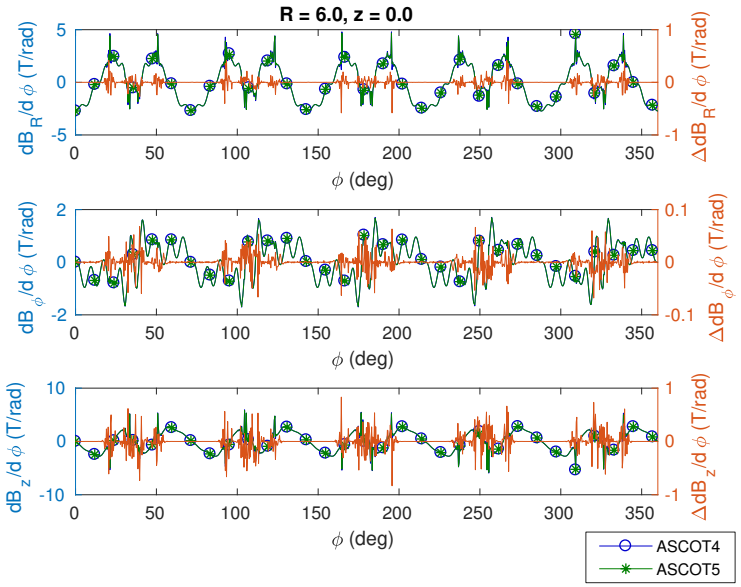

Figure 15: Profiles of the stellarator magnetic field gradient $\nabla \boldsymbol{B}$ in the φ direction. The blue lines show evaluated values for ASCOT4, and the green lines show the evaluated values for ASCOT5. The orange line shows the absolute difference (ASCOT4 - ASCOT5) between the two lines. Note the different axis used for the difference.

4.2 Radial electric field in ASCOT5

For the implementation of the radial electric field in ASCOT5, a suitable HDF5 format for the 1D electric field profiles was devised. The input includes $\frac{\partial \Phi}{\partial r_{\text{eff}}}$ as a function of ρ. Due to the definition of the effective minor radius $r_{\text{eff}} = a\rho$, if the effective minor radius a is equal to 1 m in the input, the format is equivalent to giving the profiles as $\frac{\partial \Phi}{\partial \rho}$ as a function of ρ. Functions for evaluating both the gradient of ρ and the radial electric field vector $\boldsymbol{E} = \left(E_R, E_\varphi, E_z\right)$ were implemented for ASCOT5. Evaluation of $\nabla\rho$ was done by interpolating the 3D ρ-array using the same local Hermite splines as for the magnetic field. The interpolation of the 1D electric field profiles was done using a simple linear interpolation routine.

To validate the implementation of the radial electric field E_{rad}, 1D profiles of $\nabla\rho$, as well as the electric field components, were calculated for the high-mirror scenario with both ASCOT4 and ASCOT5, similarly to section 4.1. The electric field profile consisted of 51 points in the radial direction.

Good agreement for the radial coordinate ρ was found between ASCOT4 and ASCOT5, with absolute deviations in the order of 10^{-3} that can be attributed to the different interpolation methods. The differences in $\nabla\rho$ were more significant, and the absolute difference reached as much as 10 % of the value of the gradient at some points. Similarly as for the magnetic field gradient, the interpolation of $\nabla\rho$ is more sensitive to the interpolation method. An additional source of error is that the splines representing $\nabla\rho$ oscillate near the LCFS. The reason for this is that ρ is not defined

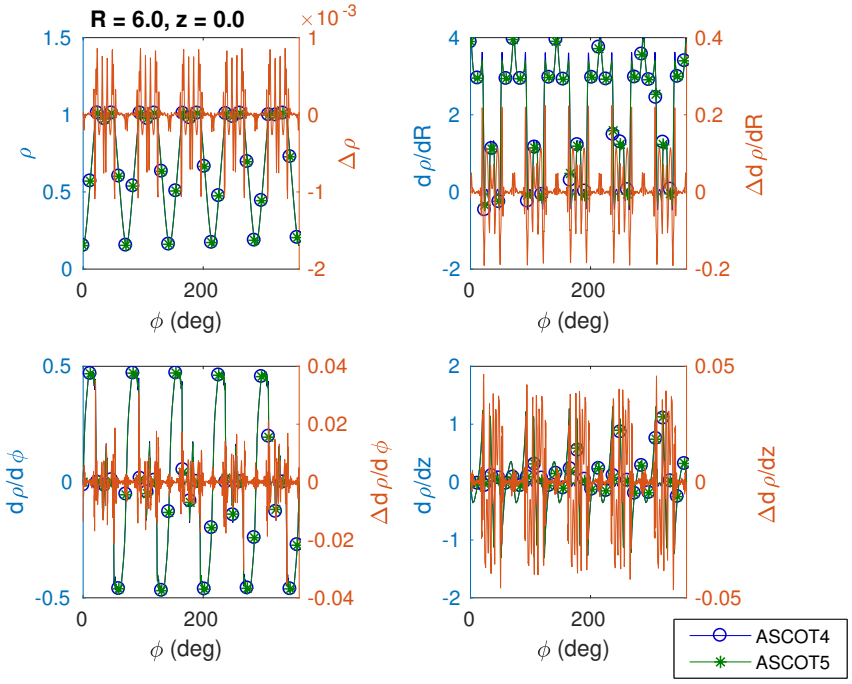

Figure 16: Profiles of the stellarator radial coordinate ρ and its gradient $\nabla\rho$ in the φ direction. The blue lines show evaluated values for ASCOT4, and the green lines show the evaluated values for ASCOT5. The orange line shows the absolute difference (ASCOT4 - ASCOT5) between the two lines. Note the different axis used for the difference.

outside the LCFS, which causes a discontinuity in the second derivative of ρ.

For the radial electric field, the relative errors between ASCOT4 and ASCOT5 were significantly larger than for ρ. The results for the $\boldsymbol{E}_{\mathrm{rad}}$ benchmarking in the φ direction are shown in figure 17. One reason for this is that $\boldsymbol{E}_{\mathrm{rad}}$ is calculated from $\nabla\rho$, which is already different between ASCOT4 and ASCOT5, and the interpolation of $\frac{\partial\Phi}{\partial r_{\mathrm{eff}}}$ causes an additional error. However, the main reason for the large difference is the way the electric field is evaluated outside the LCFS. In both ASCOT4 and ASCOT5, E_{rad} is set to zero when $\rho \geq 1$. Generally, $E_{\mathrm{rad}} \neq 0$ at the LCFS, which causes the field to abruptly change to zero. The largest differences in E_{rad} are seen when ASCOT4 and ASCOT5 disagree on whether an evaluated point is inside the LCFS or not.

The results of the ρ, $\nabla\rho$, and E_{rad} evaluations in the R and z directions were similar to the benchmarking in the φ direction, and are shown in appendix A.2.

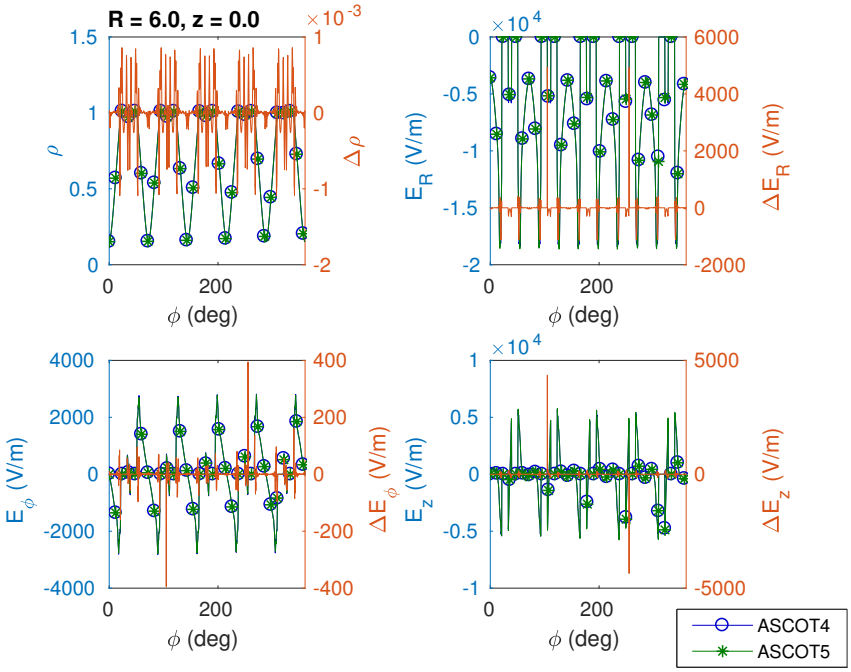

Figure 17: Profiles of the stellarator radial coordinate ρ and radial electric field $\boldsymbol{E}_{\mathrm{rad}}$ in the φ direction. The blue lines show evaluated values for ASCOT4, and the green lines show the evaluated values for ASCOT5. The orange line shows the absolute difference (ASCOT4 - ASCOT5) between the two lines. Note the different axis used for the difference.

4.3 Neutral beam injection as given by BBNBI

The performance of the neutral beam injectors of W7-X were simulated with the BBNBI code for the high mirror ratio scenario. The beam acceleration voltage was set to 55 keV, and hydrogen was used as the injected isotope. The beam powers were set according to the design parameters for the NBI device commissioning (table 3). A target number of 100 000 markers were set, a compromise between good statistics and short simulation time.

The particle shine-through in the simulated scenario was calculated to be 0.33 % of the total injected power, which is negligible compared to the design limit of the NBI beam dump. The poloidal and toroidal projections of the NBI ions show that the ions are mainly born close to the LCFS. The birth distribution of ions of the BBNBI simulation are shown in figures 18 and 19, both in cylindrical coordinates and in (ρ, ξ) space, where $\xi = v_{\parallel}/v$ is the *pitch* of the particles. The ion birth distribution (figure 19a) is clearly peaked near the LCFS, which is expected due to the flat density profile of the high-mirror scenario. It should be noted, however, that the plasma volume per unit ρ is higher near the LCFS, which partly explains the higher number of ionized particles per unit of ρ at the plasma edge. In the ξ distribution (figure 19b), four peaks corresponding to the four beam injection directions can also be clearly seen.

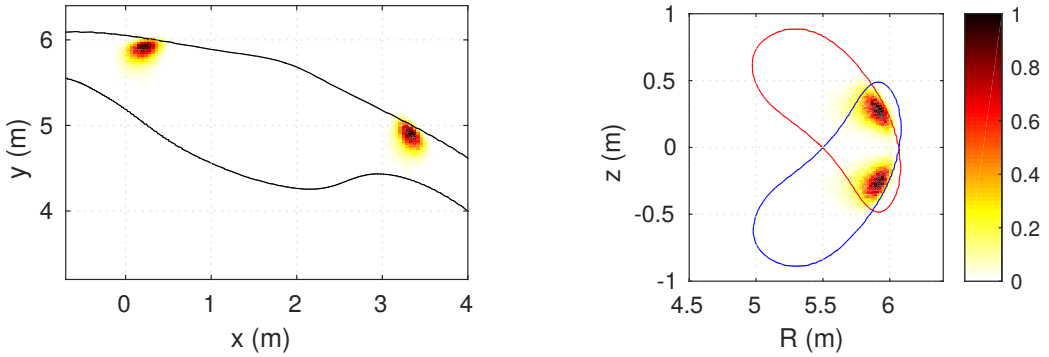

(a) (b)

Figure 18: Simulated neutral beam ionization profiles in toroidal (a) and poloidal projections (b). The red and the blue lines show the LCFS in the toroidal direction of the two beams, and the black line shows the LCFS for the z = 0 plane.

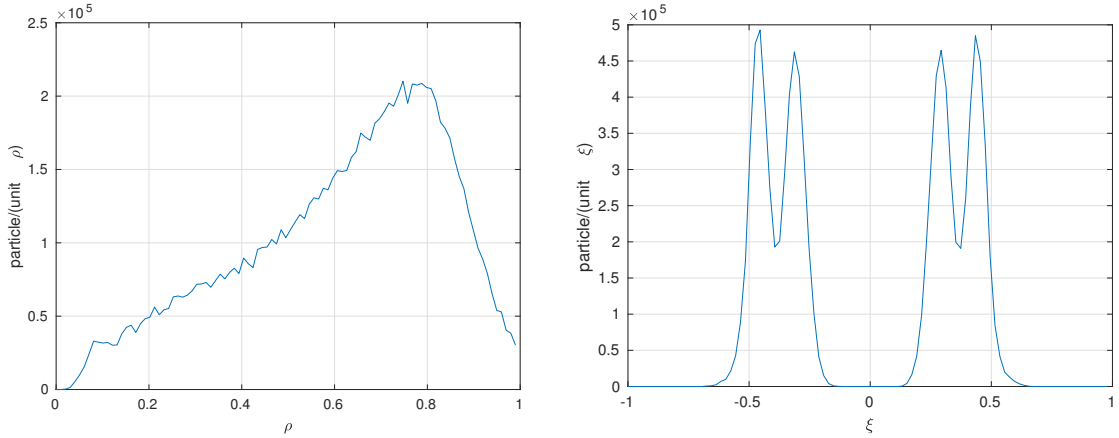

(a) (b)

Figure 19: Number density of NBI-born ions per unit of the radial coordinate ρ and pitch angle $\xi = v_{\parallel}/v$ (b).

4.4 ASCOT4 simulations of NBI ions in Wendelstein 7-X

To study the confinement of the NBI ions in the W7-X high mirror ratio scenario, ASCOT4 was used to simulate the ions until they were thermalized or collided with wall. An ion was considered thermalized when its kinetic energy was less than 1.5 times the local thermal energy (approximately 2 keV to 3 keV). An additional limit was placed on the simulation time of the ions: if the CPU time exceeded 600 second, the simulation was stopped. The complex wall model of W7-X presented in section 3.3 was used for these simulations. The 100 000 ions generated by BBNBI were simulated on the Triton cluster at Aalto University. Pure guiding-center simulation was used for these simulations in order to enable future comparisons to the ASCOT5 implementation.

The total power loss to the wall was 0.37 MW, which was 5.5 % of the NBI injected

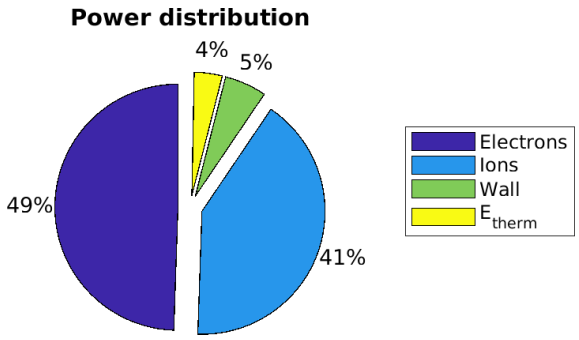

Figure 20: Power deposited by the NBI ions to the different plasma species (electrons and ions) and the wall, as well as energy remaining in the thermalized ions and ions stopped due to the simulation time, from the ASCOT4 simulation.

power. This percentage is low compared to W7-X operational scenarios that are not optimized for fast particle confinement, where earlier ASCOT simulations have predicted the loss fraction to be 6 % to 20 %, or in some cases even up to 50 % [17, 63]. Figures 20 and 21 show the overall results of the ASCOT4 simulation: the power distribution to different plasma species and the wall, and the loss fractions for several initial ρ as a function of time. Approximately 20 % more energy was deposited to the electrons than the ions of the bulk plasma.

Generally, the NBI confinement in this scenario is substantially poorer than is predicted, e.g., for the ITER tokamak, where the NBI ion loss fraction is expected to typically be just fractions of a percent, and even in the worst cases at most 2 % [64, 65, 66]. The loss fractions indicate that the ions exiting the plasma do so within the first 10^{-2} s, by which time nearly all of the particles are already either thermalized or lost. The fraction of lost particles is a strong function of the initial radial coordinate ρ_0: for $\rho_0 \approx 0.7$, approximately 6 % of the particles are lost, whereas for $\rho_0 \approx 0.9$ the corresponding fraction is over 22 % (figure 21). This suggests that the confinement of fast ions is much worse for NBI ions born near the LCFS than in the core.

The highest local wall loads are generally seen for θ =25° to 75°. This angle corresponds to the region above the magnetic axis on the outboard side of the torus. Figure 22 shows the power loads to the W7-X wall as a function of the toroidal and poloidal angles. The wall loads exhibit a five-fold periodic nature, which is expected due to the five identical toroidal periods in W7-X. The wall load pattern is otherwise stellarator-symmetric, but the magnitude of the wall loads is lower below the midplane. This implies that there is a stellarator antisymmetric component to the wall loads in W7-X. The reason for this is presumably the stellarator antisymmetric nature of the ∇B drift. A histogram of the wall area with given per-wall-element wall loads is shown in figure 23. Most of the local power loads in the high mirror scenario are in the range of 10 kW m^{-2} to 10^3 kW m^{-2}. By contrast, figure 22 shows that the highest per-element heat loads can be up to 10^5 kW m^{-2}. These results together indicate that the area hit by the largest local wall-loads is small.

One of the most important goals of NBI operation, as well as predictive modeling,

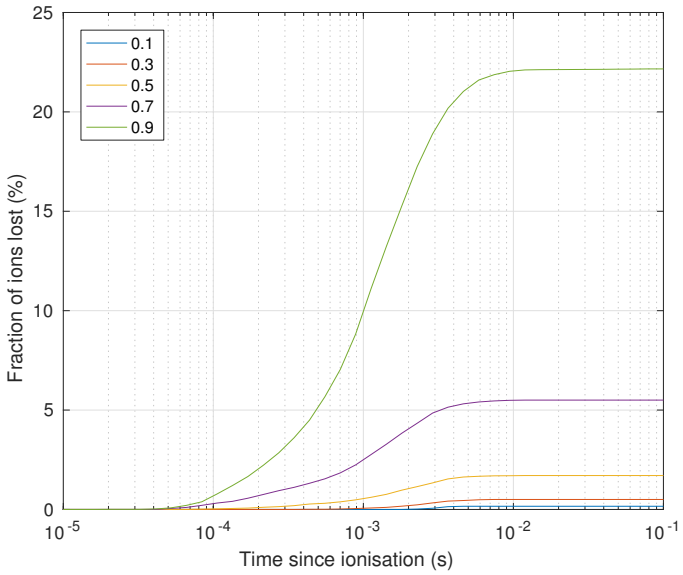

Figure 21: Loss fractions of NBI ions as calculated by ASCOT4. The different colored lines correspond to ions born near a specific value of the initial minor radius coordinate ρ_0.

is to ensure that the vulnerable components are not exposed to significant fast ion wall loads. The W7-X wall model used in this simulation includes information of the wall component type for each individual triangle in the wall model, as shown in figure 12. Figure 24 shows the power load to each individual wall triangle hit by NBI ions, grouped by component type. The power loads are concentrated on the baffle, closure, shield, and target elements. For the W7-X plasma facing components, the steady-state heat load capacity varies from $200\,\mathrm{kW\,m^{-2}}$ for the wall panels, to $10\,\mathrm{MW\,m^{-2}}$ for the high heat-flux divertor [67]. There are other components in the device not designed for high heat loads, such as the closure, vacuum vessel, diagnostics ports, and pumping slits [67]. These components might get hit by the NBI ions as well, and are particularly vulnerable to any power loads.

For all of the component types, the observed maximum wall loads are much higher than the design capacity of the W7-X components. However, it should be noted that the wall loads to individual wall elements are calculated by dividing the energy of the wall-hitting ions by the area of the element. The deficiency of this method is that the maximum per-element wall loads converge slowly with increasing number of simulation markers. Earlier ASCOT simulations have suggested that the maximum local wall loads converge only with approximately 10^8 test particles As such, the maximum per-element local wall loads presented here should be regarded as qualitative rather than quantitative, unlike the global wall loads which should provide a reasonable quantitative estimate.

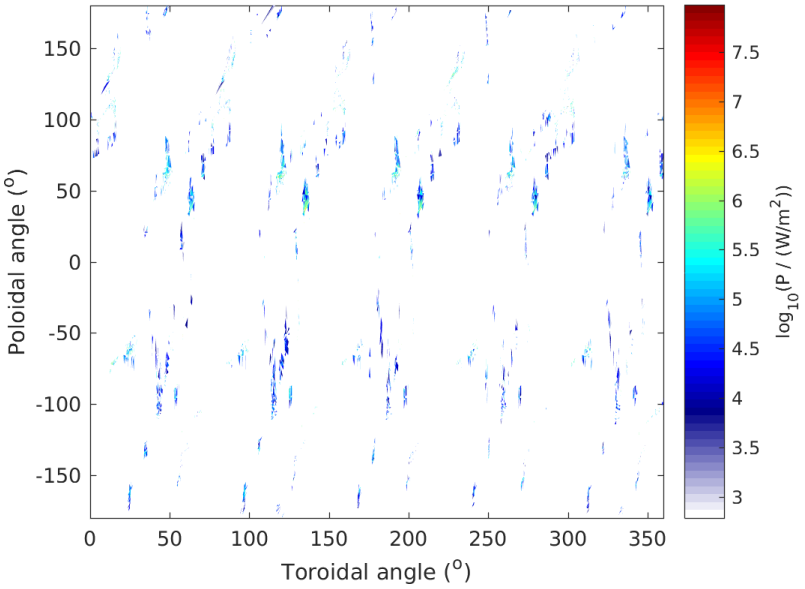

Figure 22: Power load to the W7-X wall in the high mirror ratio scenario as a function of the toroidal and poloidal angles. The color axis is the base-10 logarithm of the power per square meter.

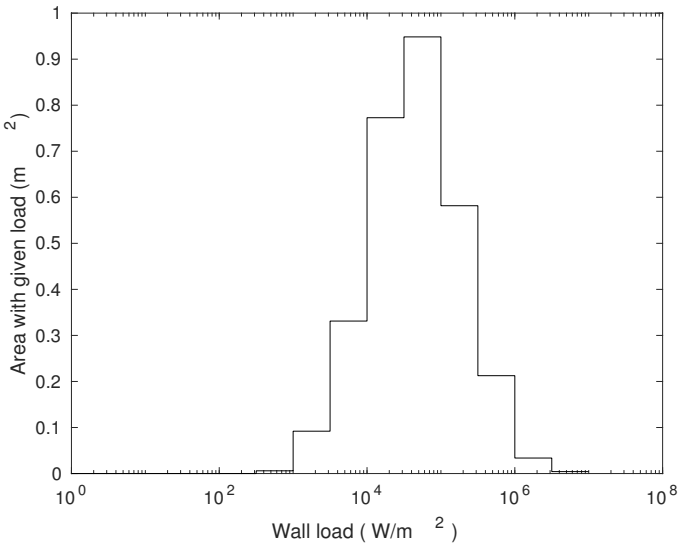

Figure 23: Histogram for the per-wall-element wall loads in the high mirror ratio scenario. The bar heights correspond to number of elements with given wall load, scaled by the element area.

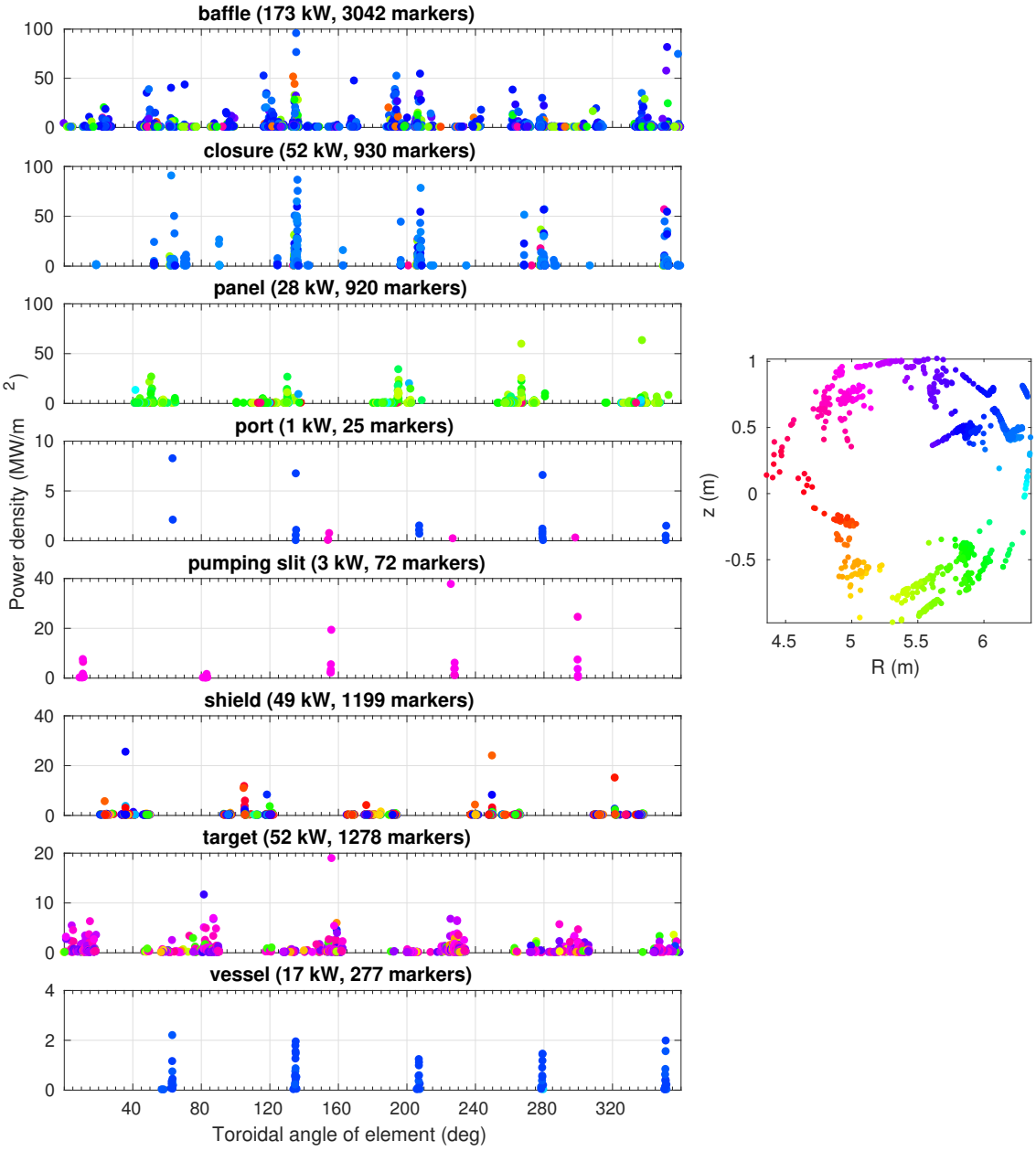

Figure 24: Toroidal scatter plot of the power loads to the W7-X wall, grouped by wall element type. Each marker represents one wall triangle, with the marker color indicating the poloidal angle of the triangle according to the legend on the right. Also shown are the total power loads per element type, as well as the number of test particles each component type. The most important element areas to monitor are the closure, vacuum vessel, diagnostics ports, and pumping slits.

5 Conclusions and future work

In this thesis we developed computational methods for assessing the impact of neutral beam injection in the Wendelstein 7-X stellarator, particularly for identifying the regions of highest power loads to the device wall. The necessary physics for stellarator neutral beam injection simulations were implemented in ASCOT5, the latest development of the ASCOT suite of codes. This included implementing the stellarator symmetric magnetic field and radial electric field. Benchmarking of the magnetic and radial electric fields between ASCOT5 and ASCOT4 showed that the differences between the two codes were between 0.01 % to 1.0 % for the magnetic field, and 0.1 % to 100 % for the electric field. The observed differences were within expected limits, because the two codes use different interpolation methods for the data.

Neutral beam injection in the W7-X high-mirror scenario was simulated with the BBNBI code to determine the birth distribution of the NBI ions. The results indicated that the beam ions are mainly born near the last closed flux surface, and that the beam shine-through is negligible in this scenario. The off-axis NBI birth distribution is characteristic for many W7-X plasmas, and is particularly problematic for fast particle confinement.

An orbit-following simulation was performed with the ASCOT4 code for the NBI ions in the high-mirror scenario. Globally, the confinement of fast particles was found to be relatively poor, with the wall power load being 5.5 % of the total injected power. However, the fast ion confinement in the studied scenario was still better than the average confinement of other operational scenarios in W7-X. The wall loads exhibited a five-fold periodic, stellarator antisymmetric pattern. Generally, the wall power loads were below the steady-state design limits of the W7-X plasma-facing components, but high local wall loads were observed. The low number of simulated test particles may bias these results, but the general outcome and the power distribution to different component types is assumed to be qualitatively consistent with experiments.

In this thesis, benchmarking between ASCOT4 and ASCOT5 was performed for the stellarator-specific magnetic field and the radial electric field implementations. The comparison was limited by the different interpolation methods used in the two codes. Implementation of the ASCOT4 spline interpolation algorithm for ASCOT5 is work in progress, and would allow definitive benchmarking of the two codes. Furthermore, as of the writing of this thesis, a complete and tested version of the ASCOT5 code has not yet been released. Because of this, full benchmarking of ASCOT4 and ASCOT5 for fast particle simulations in stellarators remains as future work.

The exact best way to mitigate the fast ion wall loads in W7-X remains an open question, as more knowledge has to be acquired on the subject. Studying different magnetic field configurations with regards to fast ion confinement is important in order to identify scenarios with good global confinement, as well as potential hot spots. Adjustments to the inward or outward shift of the magnetic field could allow

moving wall loads away from local hot spots. Fast ion wall loads could be shifted with the magnetic island control coils, designed for island control and divertor strike line sweeping. Furthermore, the acceleration voltage of the neutral beam injectors could be varied, which would have an effect on both the NBI ionization distribution as well as the width of the beam ion orbits.

Physics models still missing in ASCOT5 include charge exchange and atomic reactions, ion cyclotron resonance heating modeling, 3D arrays for plasma density and temperature, and plasma flow. Some of these models are already implemented in ASCOT4, while some would be completely new physics for ASCOT. The ICRH modeling would be especially interesting as a means of studying fast particles with a birth distribution similar to α-particles in a stellarator power plant, as no α-particles are produced in W7-X. The 3D input for plasma density and temperature, on the other hand, could enable using ASCOT to simulate impurity migration in stellarators, which has already been done for tokamaks using ASCOT4. Furthermore, the stellarator application of ASCOT5 has been limited to Wendelstein 7-X. Extending the application of ASCOT into other stellarators, such as LHD, TJ-II, and any stellarator power plant concepts is feasible.

References

[1] J. Wesson. *Tokamaks*. 4th ed. Oxford: Oxford University Press, 2011.

[2] M. Keilhacker et al. High fusion performance from deuterium-tritium plasmas in JET. *Nuclear Fusion*, 39(2):209, 1999.

[3] ITER organization. `https://www.iter.org/mach`. Accessed 2017-07-06.

[4] L. Spitzer. The Stellarator Concept. *The Physics of Fluids*, 1(4):253–264, 1958.

[5] A. F. Almagri et al. A helically symmetric stellarator (HSX). *IEEE Transactions on Plasma Science*, 27:114–115, 1999.

[6] M. Fujiwara et al. Overview of LHD experiments. *Nuclear Fusion*, 41(10):1355, 2001.

[7] C. Alejaldre et al. First plasmas in the TJ-II flexible Heliac. *Plasma Physics and Controlled Fusion*, 41(3A):A539, 1999.

[8] G. Grieger et al. Wendelstein stellarators. *Nuclear Fusion*, 25(9):1231, 1985.

[9] M Hirsch et al. Major results from the stellarator Wendelstein 7-AS. *Plasma Physics and Controlled Fusion*, 50(5):053001, 2008.

[10] Max-Planck-Institut für Plasmaphysik. *Wendelstein 7-X website*. `https://www.ipp.mpg.de/w7x`. Accessed 2017-07-01.

[11] R.C. Wolf et al. Major results from the first plasma campaign of the Wendelstein 7-X stellarator. *Nuclear Fusion*, 57(10):102020, 2017.

[12] Max-Planck-Institut für Plasmaphysik. `http://www.ipp.mpg.de/2285/en`. Accessed 2017-06-13.

[13] M. Drevlak. Thermal Load on the W7-X Vessel from NBI Losses. In: *36th EPS Conference on Plasma Phys.* (Sofia, Bulgaria). Vol. 33E. 2009, 4.211.

[14] M. McMillan and S. A. Lazerson. BEAMS3D Neutral Beam Injection Model. *Plasma Physics and Controlled Fusion*, 56(9):095019, 2014.

[15] E. Hirvijoki et al. ASCOT: Solving the kinetic equation of minority particle species in tokamak plasmas. *Computer Physics Communications*, 185:1310, 2014.

[16] O. Asunta et al. Modelling neutral beams in fusion devices: Beamlet-based model for fast particle simulations. *Computer Physics Communications*, 188:33 –46, 2015.

[17] S. Äkäslompolo et al. *ASCOT simulations of NBI wall power loads in W7-X*. EUROfusion progress report, WP15 S1 C3. 2015.

[18] F. F. Chen. *Introduction To Plasma Physics And Controlled Fusion*. 2nd. Vol. 1. New York and London: Plenum Press, 1984.

[19] M. Wakatani. *Stellarator and Heliotron Devices*. New York, Oxford: Oxford University Press, 1998.

[20] M. Eisenberg and R. Guy. A Proof of the Hairy Ball Theorem. *The American Mathematical Monthly*, 86(7):571–574, 1979.

[21] A. H. Boozer. What is a stellarator? *Physics of Plasmas*, 5(5):1647–1655, 1998.

[22] P. Helander. Theory of plasma confinement in non-axisymmetric magnetic fields. *Reports on Progress in Physics*, 77(8):087001, 2014.

[23] J. R. Cary and A. J. Brizard. Hamiltonian theory of guiding-center motion. *Reviews of Modern Physics*, 81:693–738, 2009.

[24] C. Mercier. Equilibrium and stability of a toroidal magnetohydrodynamic system in the neighbourhood of a magnetic axis. *Nuclear Fusion*, 4(3):213, 1964.

[25] W. Fundamenski. *Power Exhaust in Fusion Plasmas*. 1st. Cambridge: Cambridge University Press, 2014.

[26] G. Grieger et al. Physics optimization of stellarators. *Physics of Fluids B*, 4(7):2081–2091, 1992.

[27] M. Drevlak et al. Fast particle confinement with optimized coil currents in the W7-X stellarator. *Nuclear Fusion*, 54(7):073002, 2014.

[28] S. P. Hirshman et al. Three-dimensional free boundary calculations using a spectral Green's function method. *Computer Physics Communications*, 43(1):143–155, 1986.

[29] R. L. Dewar and S. R. Hudson. Stellarator symmetry. *Physica D: Nonlinear Phenomena*, 112(1–2):275 –280, 1998. Proceedings of the Workshop on Time-Reversal Symmetry in Dynamical Systems.

[30] Office of Science of the U.S. Department of Energy. *Opportunities in the Fusion Energy Sciences Program*. `http://sites.apam.columbia.edu/SMproceedings/12.Other/12.RelatedReports/FES_OpsAppC_Jun99.pdf`. Accessed 2017-07-03.

[31] G. Grieger et al. Physics and engineering studies for Wendelstein 7-X. In: *36th EPS Conference on Plasma Phys.* (Washington, DC). Vol. 3. IAEA, Vienna, 1990, 525–532.

[32] K. Ida et al. Experimental test of the radial force balance equation in the compact helical system. *Physics of Plasmas*, 8(1):1–4, 2001.

[33] H.-S. Bosch et al. Technical challenges in the construction of the steady-state stellarator Wendelstein 7-X. *Nuclear Fusion*, 53(12):126001, 2013.

[34] EUROfusion: Spot On JET Technology. `https://www.euro-fusion.org/fusion/jet-tech`. Accessed 2017-07-06.

[35] H.-S. Bosch et al. Physics Programme for Initial Operation of Wendelstein 7-X. *Contributions to Plasma Physics*, 50(8):687–694, 2010.

[36] T. Sunn Pedersen et al. Plans for the first plasma operation of Wendelstein 7-X. *Nuclear Fusion*, 55(12):126001, 2015.

[37] Y. Feng et al. Physics of island divertors as highlighted by the example of W7-AS. *Nuclear Fusion*, 46(8):807, 2006.

[38] R. König et al. Diagnostics design for steady-state operation of the Wendelstein 7-X stellarator. *Review of Scientific Instruments*, 81(10):10E133, 2010.

[39] A. Werner et al. W7-X magnetic diagnostics: Rogowski coil performance for very long pulses. *Review of Scientific Instruments*, 79(10):10F122, 2008.

[40] P. Kornejew et al. Design of multichannel laser interferometry for W7-X. *Review of Scientific Instruments*, 77(10):10F128, 2006.

[41] N.A. Pablant et al. Measurement of core plasma temperature and rotation on W7-X made available by the x-ray imaging crystal spectrometer (XICS). In: *Proceedings of the 41st EPS Conference on Plasma physics*. (Berlin, Germany). Vol. 38F. 2014.

[42] D. Zhang et al. Design criteria of the bolometer diagnostic for steady-state operation of the W7-X stellarator. *Review of Scientific Instruments*, 81(10):10E134, 2010.

[43] E. Pasch et al. The Thomson scattering system at Wendelstein 7-X. *Review of Scientific Instruments*, 87(11):11E729, 2016.

[44] G. Kocsis et al. Overview video diagnostics for the W7-X stellarator. *Fusion Engineering and Design*, 96:808 –811, 2015. Proceedings of the 28th Symposium On Fusion Technology.

[45] G. Duesing et al. Neutral beam injection system. *Fusion Technology*, 11(1):163–202, 1987.

[46] EUROfusion. *Scheme of the NBI principle*. `https://www.euro-fusion.org/wpcms/wp-content/uploads/2011/07/8c.jpg`. Accessed 2017-07-03.

[47] S. Suzuki et al. Attenuation of high-energy neutral hydrogen beams in high-density plasmas. *Plasma Physics and Controlled Fusion*, 40(12):2097, 1998.

[48] N. Rust et al. W7-X neutral-beam-injection: Selection of the NBI source positions for experiment start-up. *Fusion Engineering and Design*, 86(6–8):728 –731, 2011. Proceedings of the 26th Symposium of Fusion Technology.

[49] P. McNeely et al. Current status of the neutral beam heating system of W7-X. *Fusion Engineering and Design*, 88(6–8):1034 –1037, 2013. Proceedings of the 27th Symposium On Fusion Technology.

[50] R. Nocentini et al. Design of the torus interface for the neutral beam injectors of Wendelstein 7-X. *Fusion Engineering and Design*, 100:453 –460, 2015.

[51] J. Geiger. Stability analysis of Wendelstein 7-X configurations with increased mirror ratio. In: *Proceedings of the 17th International Toki Conference*. 2007, 332–335.

[52] A. Kolmogoroff. Über die analytischen Methoden in der Wahrscheinlichkeitsrechnung. *Mathematische Annalen*, 104(1):415–458, 1931.

[53] S. Äkäslompolo et al. Calculating the 3D magnetic field of ITER for European TBM studies. *Fusion Engineering and Design*, 98–99:1039 –1043, 2015. Proceedings of the 28th Symposium On Fusion Technology.

[54] O. Asunta et al. Simulations of fast ion wall loads in ASDEX Upgrade in the presence of magnetic perturbations due to ELM-mitigation coils. *Nuclear Fusion*, 52(9):094014, 2012.

[55] M. Barth et al. *Best Practice Guide Intel Xeon Phi v1.1, PRACE 2014*. `http://www.praceproject.eu/IMG/pdf/Best-Practice-Guide-Intel-Xeon-Phi.pdf`. Accessed 2017-07-03.

[56] Y. Turkin et al. Transport modelling of operational scenarios in W7-X. In: *Proceedings of the 41st EPS Conference on Plasma physics*. (Berlin, Germany). Vol. 38F. 2014, P1.086.

[57] W. I. van Rij and S. P. Hirshman. Variational bounds for transport coefficients in three-dimensional toroidal plasmas. *Physics of Fluids B: Plasma Physics*, 1(3):563, 1989.

[58] Yu. Turkin et al. Current Control by ECCD for W7-X. *Fusion Science and Technology*, 50(3):387–394, 2006.

[59] M. Drevlak et al. PIES free boundary stellarator equilibria with improved initial conditions. *Nuclear Fusion*, 45(7):731, 2005.

[60] S. Bozhenkov. private communication.

[61] M. Drevlak et al. *Power flux from NBI losses on in-vessel components in W7-X*. Tech. rep. Max-Planck-Institute for Plasma Physics, 2011.

[62] The HDF5 group. `https://support.hdfgroup.org/HDF5/`. Accessed 2017-07-04.

[63] J. Kontula et al. Predictive modelling of NBI wall loads in W7-X scenarios exhibiting vanishing bootstrap current:P2.146, 2017. Proceedings of the 44th EPS conference on Plasma Physics, Belfast, Northern Ireland (Jun. 2017).

[64] S. Äkäslompolo et al. ITER fast ion confinement in the presence of the European test blanket module. *Nuclear Fusion*, 55(9):093010, 2015.

[65] T. Kurki-Suonio et al. Effect of the European design of TBMs on ITER wall loads due to fast ions in the baseline (15 MA), hybrid (12.5 MA), steady-state (9 MA) and half-field (7.5 MA) scenarios. *Nuclear Fusion*, 56(11):112024, 2016.

[66] J. Varje et al. Effect of plasma response on the fast ion losses due to ELM control coils in ITER. *Nuclear Fusion*, 56(4):046014, 2016.

[67] R. Stadler et al. Steady-State In Vessel Components for the Wendelstein 7-X Stellarator. In: *Proceedings of the 18th International Toki Conference*. Vol. I-24. 2008, 98–102.

[68] *Proceedings of the 41st EPS Conference on Plasma physics*. (Berlin, Germany). Vol. 38F. 2014.

A Appendix

A.1 Magnetic field interpolation results

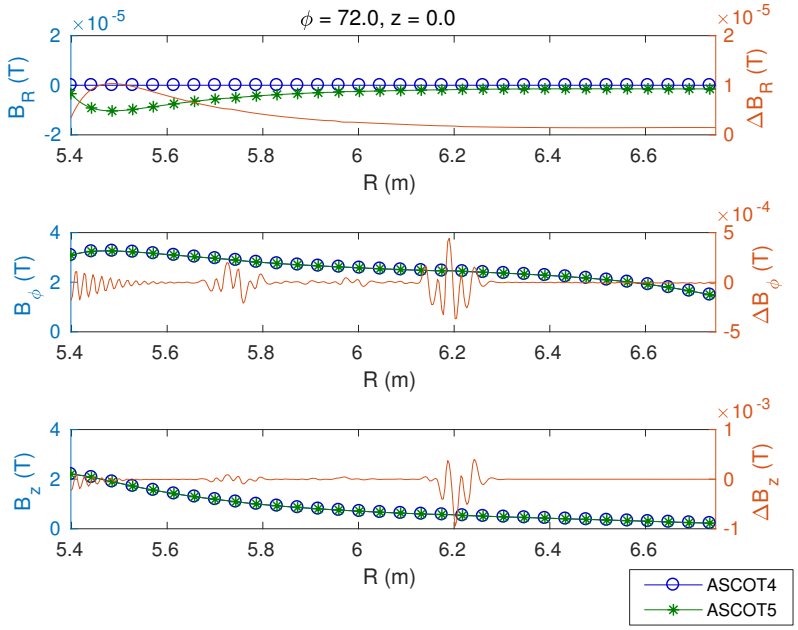

Figure A1: Interpolated slices of the stellarator magnetic field B in the R direction.

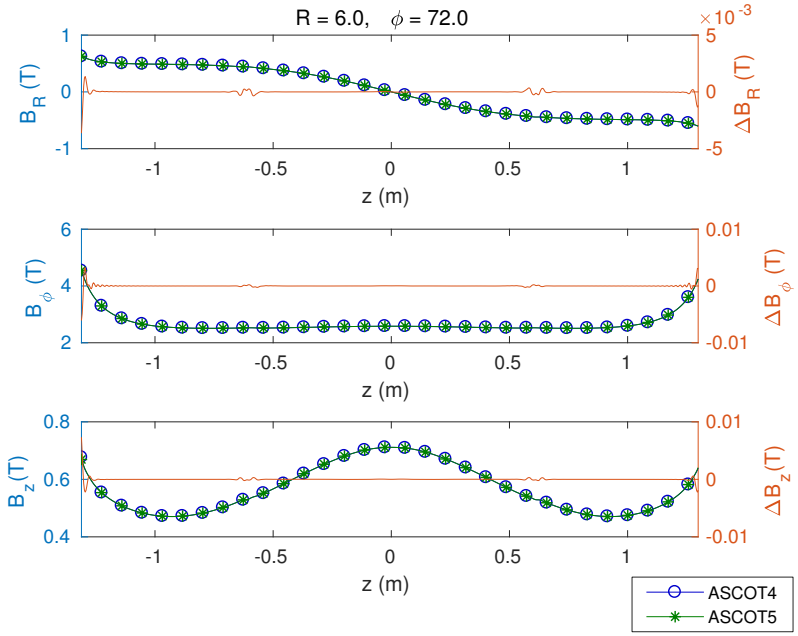

Figure A2: Interpolated slices of the stellarator magnetic field B in the z direction.

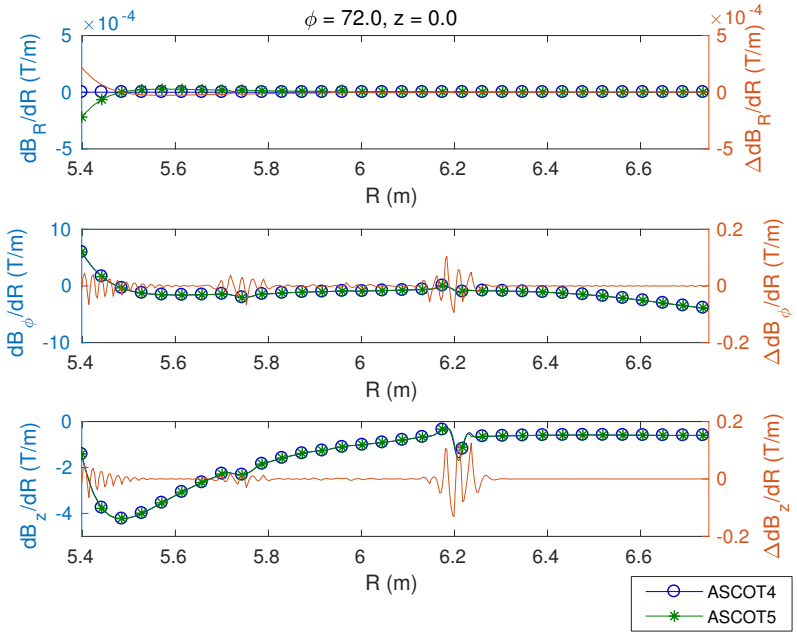

Figure A3: Interpolated slices of the stellarator magnetic field gradient $\nabla \boldsymbol{B}$ in the R direction.

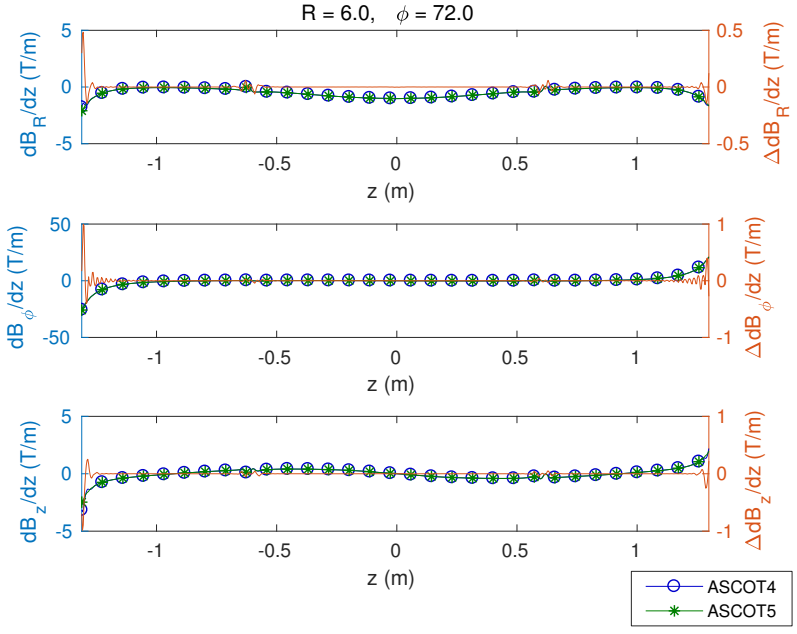

Figure A4: Interpolated slices of the stellarator magnetic field gradient $\nabla \boldsymbol{B}$ in the z direction.

A.2 Electric field interpolation results

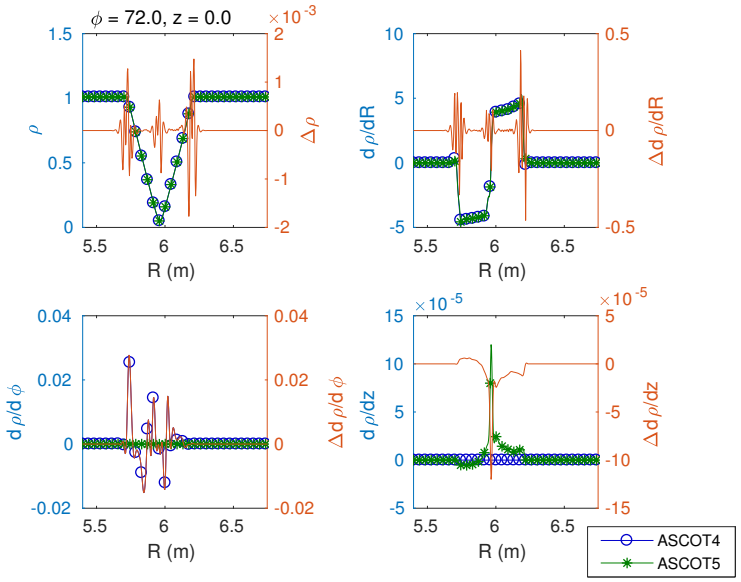

Figure A5: Interpolated slices of the stellarator radial coordinate ρ and $\nabla\rho$ in the R direction.

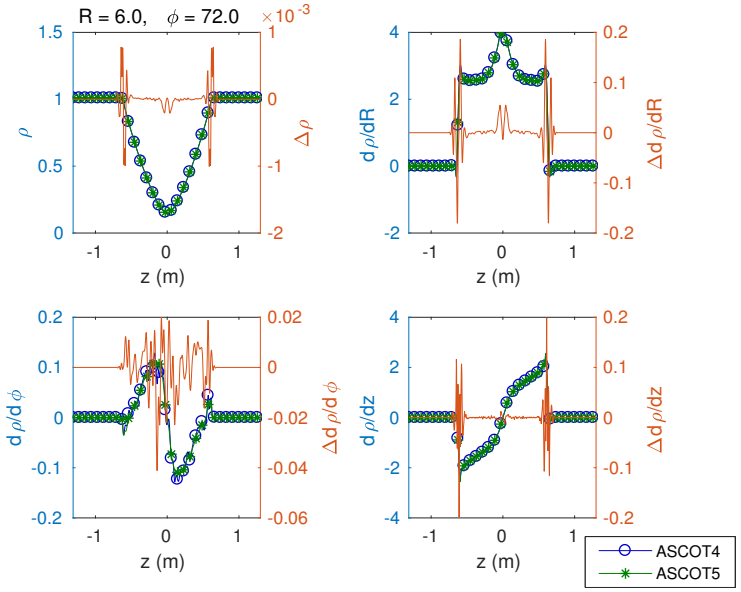

Figure A6: Interpolated slices of the stellarator radial coordinate ρ and $\nabla\rho$ in the z direction.

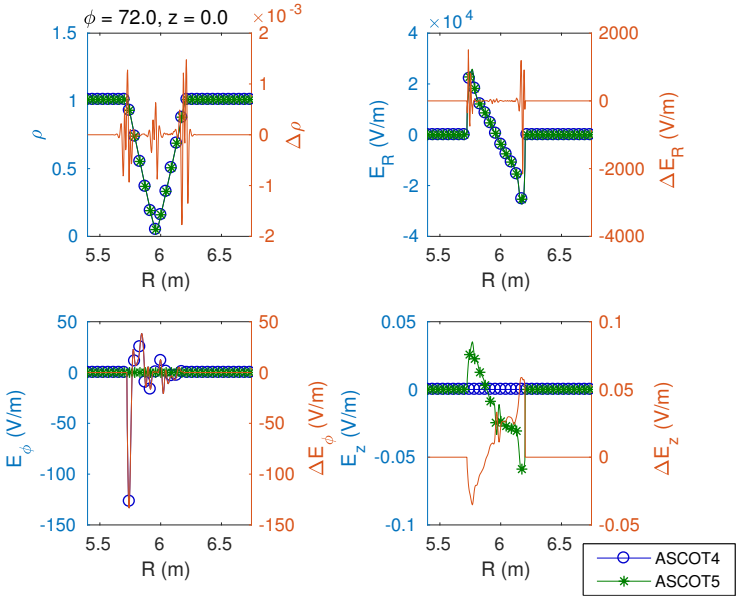

Figure A7: Interpolated slices of the stellarator radial coordinate ρ and radial electric field $\boldsymbol{E}_{\mathrm{rad}}$ in the R direction.

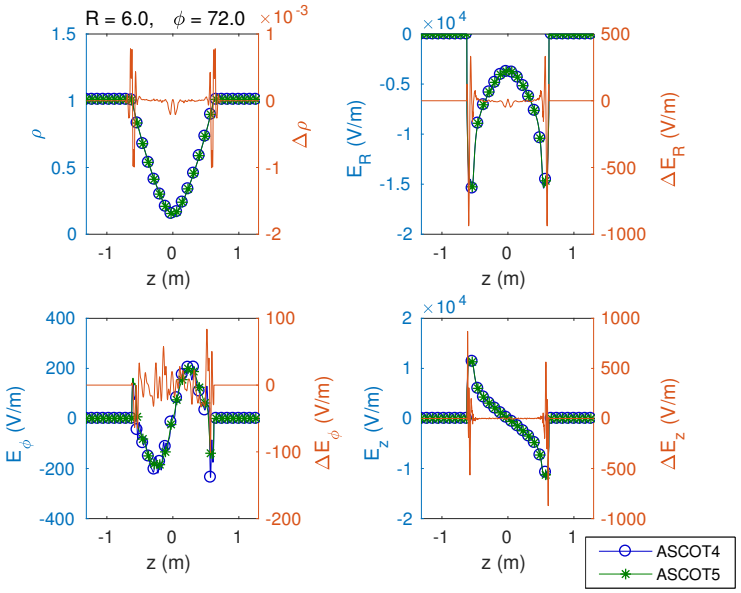

Figure A8: Interpolated slices of the stellarator radial coordinate ρ and radial electric field $\boldsymbol{E}_{\mathrm{rad}}$ in the z direction.